minerals

MDPI

Article

Petrogenesis and Tectonic Implications of the Neoproterozoic Peraluminous Granitic Rocks from the Tianshui Area, Western Margin of the North Qinling Terrane, China: Evidence from Whole-Rock Geochemistry and Zircon U–Pb–Hf–O Isotopes

Gang Yang, Juan Zhang *, Hongfu Zhang, Zhian Bao and Abing Lin

State Key Laboratory of Continental Dynamics, Department of Geology, Northwest University, Xi'an 710069, China; yg1392874237@gmail.com (G.Y.); hfzhang@mail.igcas.ac.cn (H.Z.); 20134526@nwu.edu.cn (Z.B.); ablin@nwu.edu.cn (A.L.)

* Correspondence: zjuan@nwu.edu.cn

Abstract: The source and petrogenesis of peraluminous granitic rocks in orogenic belts can provide insights into the evolution, architecture, and composition of continental crust. Neoproterozoic peraluminous granitic rocks are sporadically exposed in the Tianshui area of the western margin of the North Qinling Terrane (NQT), China. However, the source, petrogenesis, and tectonic setting of these rocks still remain unclear, which limits our understanding of the Precambrian tectonic and crustal evolution of the Qinling Orogenic Belt (QOB). Here, we determined the whole-rock geochemical compositions and in situ zircon U–Pb ages, trace-element contents, and Hf–O isotopic compositions of a series of peraluminous granitic mylonites and granitic gneisses in the Tianshui area at the west end of North Qinling. Zircon U–Pb dating revealed that the protoliths of the studied granitic mylonites and granitic gneisses crystallized at 936–921 Ma. The granitic rocks displayed high A/CNK values (1.12–1.34) and were enriched in large-ion lithophile elements (e.g., Rb, Ba, Th, U, and K) and light rare earth elements, and they were depleted of high-field-strength elements (e.g., Nb, Ta, and Ti). These rocks showed variable zircon $\varepsilon_{Hf}(t)$ (−12.2 / 9.7) and $\delta^{18}O$ (3.56‰ / 11.07‰) values, suggesting that they were derived from heterogeneous crustal sources comprising predominantly supracrustal sedimentary rocks and subordinate igneous rocks. In addition, the U–Pb–Hf isotopic compositions from the core domains of inherited zircons were similar to those of detrital zircons from the Qinling Group, suggesting that the Qinling Group was an important crustal source for the granitic rocks. The lithological and geochemical features of these granitic rocks indicate that they were generated by biotite dehydration melting of heterogeneous sources at lower crustal depths. Combining our results with those of previous studies, we suggest that the NQT underwent a tectonic transition from syn-collision to post-collision at 936–874 Ma in response to the assembly and breakup of the Rodinia supercontinent.

Keywords: Neoproterozoic; western margin of the NQT; zircon U–Pb–Hf–O isotopes; granitic rocks; petrogenesis; source nature

Citation: Yang, G.; Zhang, J.; Zhang, H.; Bao, Z.; Lin, A. Petrogenesis and Tectonic Implications of the Neoproterozoic Peraluminous Granitic Rocks from the Tianshui Area, Western Margin of the North Qinling Terrane, China: Evidence from Whole-Rock Geochemistry and Zircon U–Pb–Hf–O Isotopes. *Minerals* **2022**, *12*, 910. https://doi.org/10.3390/min12070910

Academic Editor: Sung Hi Choi

Received: 13 June 2022
Accepted: 18 July 2022
Published: 20 July 2022

1. Introduction

Orogenic belts with Precambrian basement comprising pre-orogenic components are important sites of crustal growth and reworking [1–3]. Peraluminous granites are present in many orogenic belts, providing valuable information regarding the early tectonic and crustal evolution of the orogenic belts [4–9].

The Qinling Orogenic Belt (QOB) is located between the North China and South China blocks, and it is a major component of the Central Orogenic Belt (Figure 1a). Numerous studies have shown that the QOB underwent multistage metamorphism and magmatism [10–17]. Neoproterozoic peraluminous granitic rocks in the eastern part of the North

Qinling Terrane (NQT) have been recognized and widely investigated (Table 1; [18–20]). In contrast, the Neoproterozoic peraluminous granitic rocks in the western part of the NQT have received much less attention. The western margin of the NQT is located near the triple junction of the Yangtze Craton, North China block, and Tibetan Plateau (Figure 1a). The closure of the Paleo-Tethys Ocean, amalgamation between the North China block and the South China block, and the Tibetan Plateau uplift since the Cenozoic further complicated the geology of the region [21–24]. Precambrian magmatism in the western margin of the NQT is at a relative low degree of preservation. Therefore, the Neoproterozoic peraluminous granitic rocks in the region can provide critical constraints on the tectonic evolution of the QOB and the identity of unexposed basement.

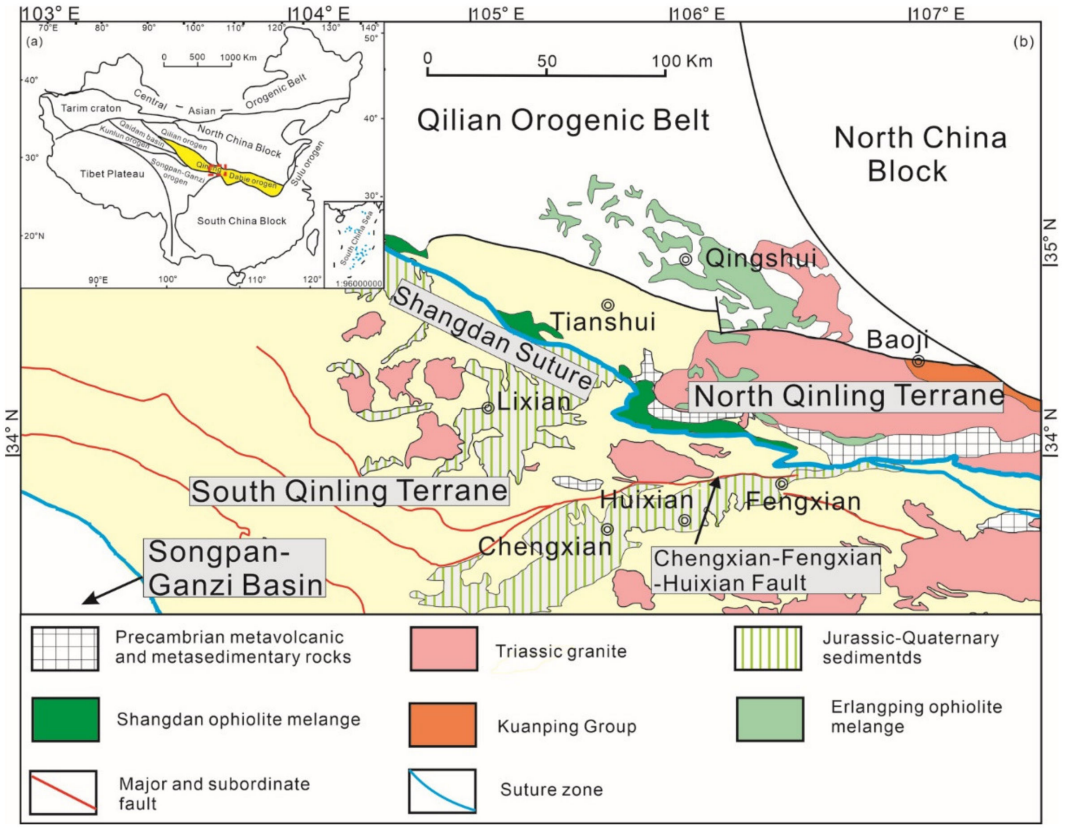

Figure 1. (**a**) Tectonic map of China (modified after [14]); (**b**) Simplified geological map of the western margin of the NQT (modified after [14,25]).

Table 1. A summary of the localities, lithology, and protolith ages of the early Neoproterozoic granitic rocks in the QOB.

Location	Rock Type	Protolith Age (Ma)	Analytical Method	Reference
West Qinling				
Wushan	Granitic mylonite	927 ± 10–933 ± 7	LA-ICPMS	This study
Xinyang	Granitic gneiss	921 ± 9–936 ± 16	LA-ICPMS	This study
Yuanlong	Granitic gneiss	924 ± 9–937 ± 8	LA-ICPMS	This study
Wushan	Granitic mylonite	951 ± 18	SHRIMP	[26]
Wushan	Granitic mylonite	910 ± 5	LA-ICPMS	[27]
Yuanlong	Biotite monzonite granitic gneiss	915 ± 8	LA-ICPMS	[28]
Xinyang	Biotite monzonite granitic gneiss	936 ± 4–979 ± 5	LA-ICPMS	[28]
Yuanlong	Granitic gneiss	924 ± 3	LA-ICPMS	[29]

Table 1. *Cont.*

Location	Rock Type	Protolith Age (Ma)	Analytical Method	Reference
East Qinling				
Songshugou	Garnet plagioamphibolite	983 ± 140	Sm-Nd	[30]
Dehe	Biotite adamellite	964 ± 5–943 ± 18	TIMS/SHRIMP	[31]
Caiao	Granodiorite	889 ± 10	LA-ICPMS	[32]
Huangbaiyu	Granodiorite	670 ± 40	Rb-Sr	[33]
Lajimiao	Diorite	973 ± 60	LA-ICPMS	[34]
Lianghekou	Monzonite granite gneiss	852 ± 2	U-Pb isochron	[35]
Niujiaoshan	Granitic gneiss	959 ± 4	TIMS	[36]
Xilaoyu	Biotite granite gneiss	956 ± 8	TIMS	[37]
Niujiaoshan	Dimica monzonite granite gneiss	955 ± 5	TIMS	[37]
Guojiaping	Quartz monzonite gneiss	953 ± 14	SHRIMP	[37]
Dehe	Biotite monzonite granite gneiss	943 ± 18–971 ± 10	SHRIMP/TIMS	[37]
Zhaigen	Biotite granite	914 ± 10	SHRIMP	[37]
Taibaigong	Tonaldiorite gneiss	863 ± 17–911 ± 18	TIMS/SHRIMP	[37]
Huangtuniu	Biotite granite gneiss	844 ± 4	TIMS	[37]
Niujiaoshan	Gneissic granite	955 ± 13	SHRIMP	[38]
Dehe	Biotite monzonite granite gneiss	948 ± 9	LA-ICPMS	[19]
Fangzhuang	Granitic mylonite	933 ± 9	SIMS	[19]
Shicaogou	Biotite adamellite	925 ± 11	LA-ICPMS	[39]
Xilaoyu	Granodioritic gneiss	956 ± 8	ID-TIMS	[40]
Niujiaoshan	Two-mica granitic gneiss	955 ± 5	ID-TIMS	[40]
Dehe	Biotite granitic gneiss	943 ± 18	SHRIMP	[40]
Guanshan	Biotite granitic gneiss	929 ± 16	SHRIMP	[40]
Zhaigen	Biotite granitic gneiss	914 ± 10	SHRIMP	[40]
Dehe	Biotite monzonitic gneiss	925 ± 23	LA-ICPMS	[20]
Zhaigen	Granite	902 ± 7	LA-ICPMS	[41]
Fangzhuang	Granite	934 ± 9	LA-ICPMS	[41]
Dehe	Granite	942 ± 7	SHRIMP	[41]
Mashankou	Granitic gneiss	929 ± 7	LA-ICPMS	[42]

In this study, we present new whole-rock geochemical compositions and in situ zircon U–Pb–Hf–O isotopic and trace elemental data for Neoproterozoic granitic mylonites and granitic gneisses from the Tianshui area of the NQT to constrain their source, petrogenesis, and tectonic setting. We used our results together with a compilation of U–Pb–Hf–O isotopic data for early Neoproterozoic granitic rocks from the NQT to reconstruct the early evolution of the QOB (Table 1).

2. Regional Geology and Petrography

The QOB is located in the central part of the Central Orogenic Belt and was formed by the collision between the North China block and the South China block (Figure 1a; [43]). The QOB can be subdivided by the Shangdan Fault into two mountain chains: the South Qinling Terrane and the NQT (Figure 1b; [11–13,43]. The NQT connects the Qilian to the west and the Dabie to the east (Figure 1b).

Precambrian basement is only rarely exposed in the western part of the NQT. The oldest exposed crystalline basement of the region is the Paleoproterozoic Qinling Group, which is composed mainly of gneisses, amphibolites, and marbles [11]. Zircon U–Pb ages of 2267–2172 Ma have been reported for the gneisses [13]. The vast exposed strata of the west-

ern part of the NQT consist primarily of Devonian–Cretaceous marine metasedimentary rocks [44] that are intruded by voluminous Mesozoic granitic plutons [45–47].

Neoproterozoic granitic rocks are widespread in the NQT. On the basis of mineral assemblages, textures, and geochemical characteristics, these granitic rocks are classified as strongly deformed S-type, weakly deformed I-type, and nondeformed A-type granitoids [48–51]. These three groups of rocks were formed in three stages at 980–880, 870–844, and 830–630 Ma, respectively [19,48,51]. Early Neoproterozoic peraluminous granitic gneisses (e.g., the Dehe, Fangzhuang, Niujiaoshan, and Zhaigen) in the eastern part of the NQT are interpreted to have formed in a syn-collisional tectonic regime associated with the assembly of the Rodinia supercontinent [48–51]. Early Neoproterozoic granitic rocks in the western margin of the NQT are distributed sporadically in several areas including Wushan, Yuanlong, and Xinyang [27–29,52]. Recent zircon U–Pb analyses of these rocks have yielded protolith ages of 910–978 Ma [26–29]. Numerous contemporary peraluminous granitic gneisses have been recognized in adjacent blocks including the Altun–Qilian–Kunlun–North Qaidam (AQKNQ) region [53–61].

The Neoproterozoic mafic–ultramafic rocks are lower in volume compared with the granitic rocks in the NQT. The Songshugou mafic–ultramafic complex is the largest peridotite block in the QOB, which is located on the northern side of the Shangdan suture [62]. The peridotites show Re–Os model ages of 1240~800 Ma [63–65], which are interpreted to be fragments of the oceanic lithosphere [62,64,66] or a mantle wedge in a forearc setting [63,67]. The meta-mafic rocks, including (retro-) eclogites and (garnet-) amphibolites, in the Guanpo–Zhaigen–Shuanghuaishu–Xixia–Songshugou areas yielded protolith ages of 840~750 Ma [68–73].

For the present study, we collected three granitic mylonite samples from the Wushan area and three granitic gneiss samples from each of the Yuanlong and Xinyang areas. The Wushan granitic mylonite is located in the ductile shear zone of the Wushan ophiolite unit in the northwestern margin of the NQT (Figure 2a). The mylonite is located adjacent to marble to the north and metabasalt to the south (Liang, 2017). The mylonite is light grey, shows a mylonitic foliation and lineation, and is composed of quartz (ca. 50 vol%), K-feldspar (ca. 30 vol%), biotite (ca. 10 vol%), and muscovite (ca. 10 vol%) (Figure 3a,d). The accessory minerals are mainly apatite, zircon, and garnet. K-feldspar grains are of an augen structure. Quartz grains display anhedral irregular undulatory extinction and are distributed along the K-feldspar grains. Kinked and elongated biotite and muscovite grains form a directional band of flaky mineral aggregate.

The Yuanlong granitic gneiss is located on the northern side of the Weihe River between the Boyang and Yuanlong areas (Figure 2b). This granitic gneiss is in contact with the Neoproterozoic Huluhe Group to the north and the early Paleozoic Caotangou Group to the south [29]. The samples were medium to coarse grained with a gneissic structure and were composed of quartz (ca. 45 vol%), plagioclase (ca. 35 vol%), biotite (ca. 10 vol%), and muscovite (ca. 10 vol%) (Figure 3b,e), with minor amounts of apatite and zircon. Plagioclase is anhedral and granular, while quartz is elongated and shows wavy extinction. Biotite together with muscovite forms a directional band of flaky mineral aggregate.

The Xinyang granitic gneiss is located in the Xiweizi ravine to the south of the Weihe River near Xinyang Town (Figure 2c). The samples were composed predominantly of quartz (ca. 40 vol%), plagioclase (ca. 30 vol%), K-feldspar (ca. 10 vol%), biotite (ca. 10 vol%), and muscovite (ca. 10 vol%) (Figure 3c,f), with accessory ilmenite, zircon, apatite, and garnet. Plagioclase and K-feldspar are subhedral–euhedral, while quartz is mostly anhedral and shows wavy extinction. Biotite together with muscovite forms a directional band of flaky mineral aggregate.

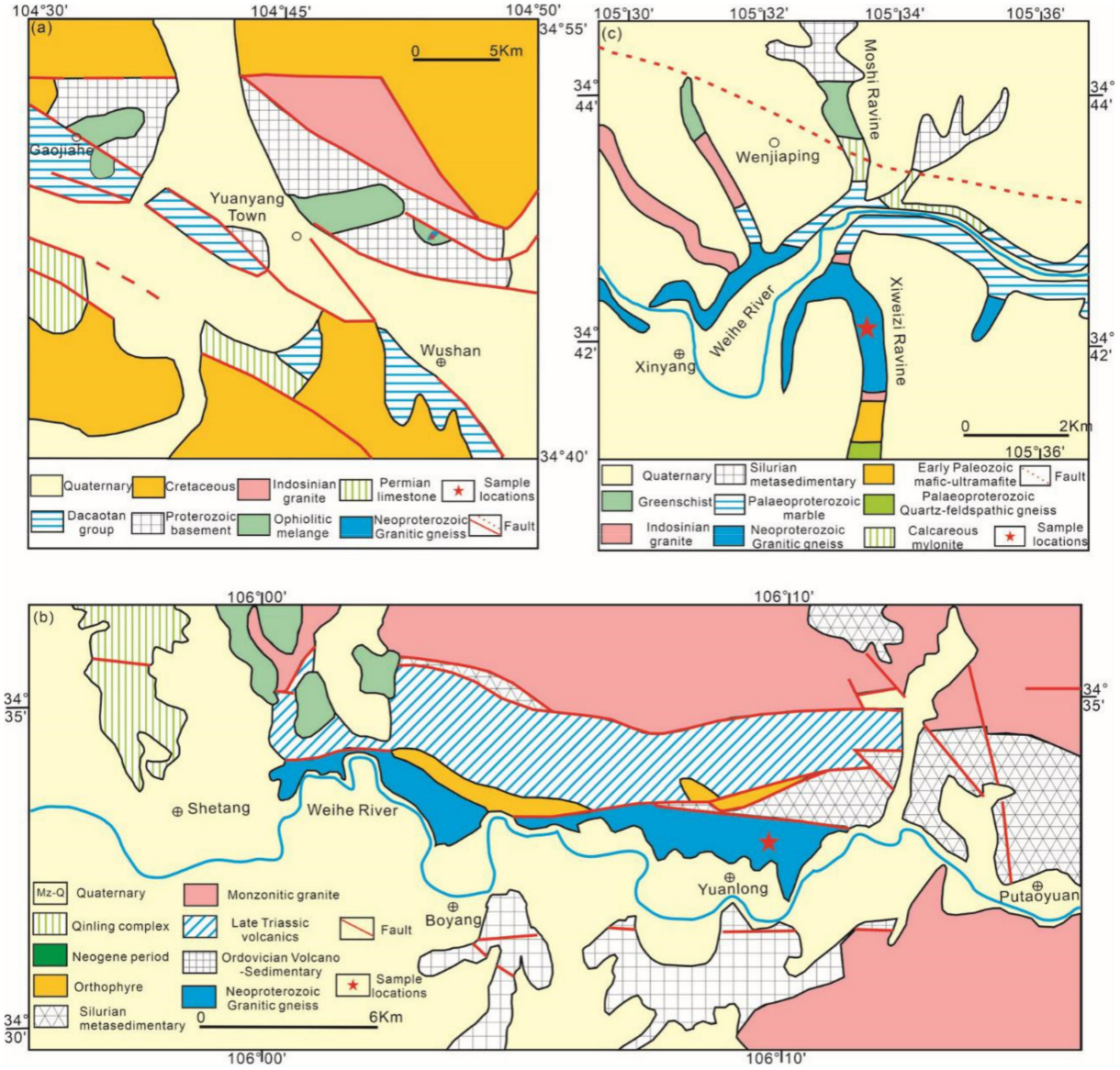

Figure 2. (**a**) Geological map of the Wushan area (modified after [26]); (**b**) geological map of the Yuanlong area (modified after [52]); (**c**) geological map of the Xinyang area (modified after [52]).

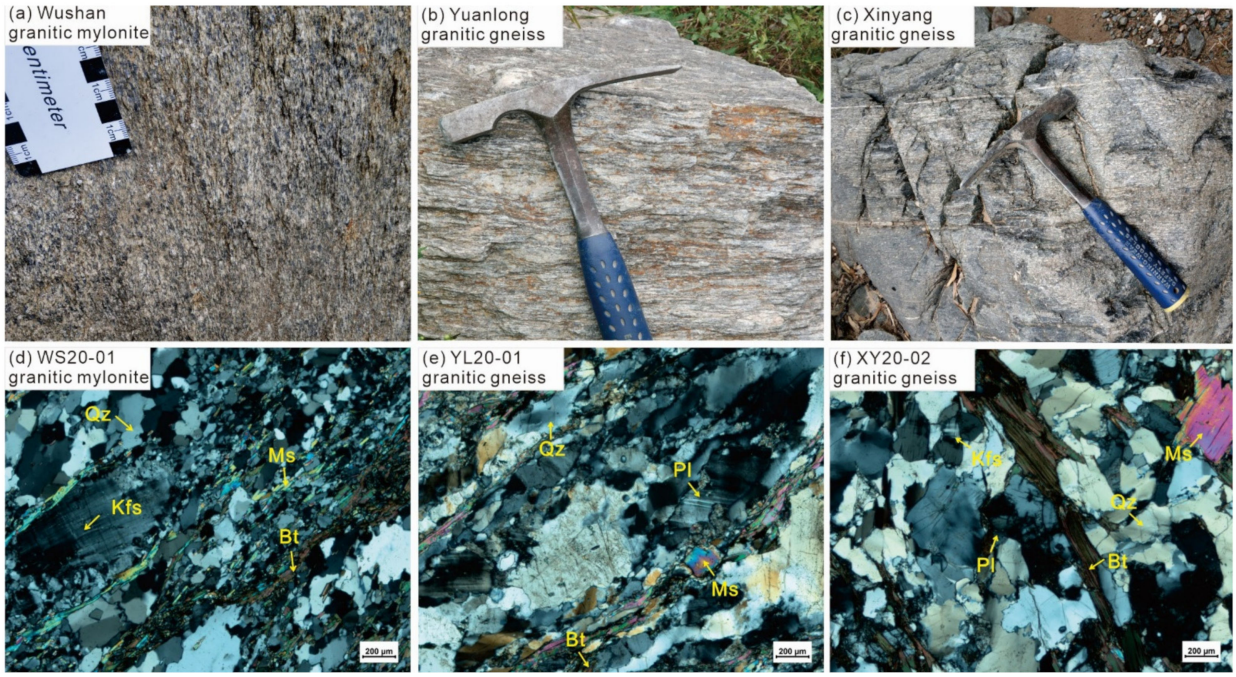

Figure 3. Field photographs (**a**–**c**) and photomicrographs (**d**–**f**) of granitic mylonites and granitic gneisses from the Wushan, Yuanlong, and Xinyang areas. Qz—quartz; Pl—plagioclase; Ms—muscovite; Kfs—K-feldspar; Bt—biotite.

3. Analytical Methods

Whole-rock major and trace element and zircon U–Pb isotope analyses were performed at the State Key Laboratory of Continental Dynamics, Northwest University, Xi'an, China. In situ zircon O isotope analyses were conducted at the Guangzhou Institute of Geochemistry, Chinese Academy of Sciences, Guangzhou, China. Zircon Lu–Hf isotope analyses were performed at the Xi'an Geological Survey Center of the China Geological Survey, Xi'an, China.

3.1. Whole-Rock Major and Trace Element Analyses

Whole-rock major element contents were analyzed by X-ray fluorescence (XRF) using a Rigaku RIX2100 instrument (Rigaku, japan). The Chinese national rock standard, GBW07105, and the United States Geological Survey (USGS) standard, BCR-2, were used as reference materials. The uncertainty regarding the major element contents was less than 2%. Whole-rock trace element contents were measured by inductively coupled plasma mass spectrometry (ICP–MS) using an Agilent 7500A instrument (Agilent, Santa Clara, CA, USA), with USGS reference materials (i.e., BHVO-2, AGV-2, BCR-2, and GSP-2) used as standard samples to estimate the analytical precision. The accuracy and precision of the whole-rock trace elements were better than 5% and 10%, respectively.

3.2. Preparation and Imaging of Zircons

The internal structures of zircons commonly yield valuable geological information. Zircons were observed prior to analyses of O and Lu–Hf isotopes and U–Pb dating to characterize their internal structure and to select analytical spots for isotopes and dating. Accordingly, the selection and morphology of zircons are particularly important. Rock samples were first mechanically crushed in the laboratory, following which whole zircon crystals were separated using conventional heavy liquid and magnetic techniques. Clear zircons without inclusions or cracks were handpicked under a binocular microscope. The selected zircons were mounted on a 20 mm diameter disc with epoxy resin and polished to expose the crystal interiors. An FEI Quanta 400 FEG scanning electron microscope together

with an Oxford Instruments energy-dispersive spectroscopy system and a Gatan CL3+ detector were used to obtain cathodoluminescence (CL) images.

3.3. In Situ Zircon O Isotope Analyses

In situ zircon O isotopes were measured using a Cameca IMS 1280-HR secondary ion mass spectrometry (SIMS) instrument (Cameca, France) in GIG. For analyses during this study, a beam diameter of ca. 10 μm and an energy intensity of 2–3 nA were used. Penglai ($\delta^{18}O$ = 5.31‰ ± 0.1‰; [74]) were used as a standard to correct instrument bias. A $^{133}Cs+$ ion source with a strength of ca. 2 nA was used to bombard the sample with an accelerating voltage of 10 kV, and negative secondary ions were extracted with an accelerating voltage of −10 kV. Two Faraday cups were used to receive ^{16}O and ^{18}O. Qinghu was also analyzed to monitor the data quality. During our session, the determined weighted mean $\delta^{18}O$ values of the Qinghu was 5.54‰ ± 0.25‰, the same as the recommended values within error [74,75]. The detailed experimental procedures and data reduction techniques have been described by Yang et al. (2018, 2019) [76,77].

3.4. In Situ Zircon U–Pb Dating and Trace Element Analyses

In situ zircon U–Pb isotopes and trace elements were measured with a 30 μm beam diameter using an Agilent 7700a ICP–MS instrument (Agilent, Santa Clara, CA, USA) coupled to a GeoLas 2005 ArF-excimer laser (Coherent, Inc., Santa Clara, CA, USA) operating at a 193 nm wavelength and 1–20 Hz denudation frequency. Detailed procedures and operating conditions for the LA–ICP–MS U–Pb dating are described by Yuan et al. (2004) [78]. GLITTER (VER 4.0) software developed by W. L. Griffin of Macquarie University was used for data processing and age calculations. A standard zircon GJ-1 was used as the external standard for isotope ratio correction, and element contents were calculated using NIST 610 as the external standard and ^{29}Si as the internal standard. Correction for common Pb followed Andersen (2002) [79]. Calculation of the weighted mean ages and drawing of the concordia diagrams were performed using ISOPLOT 3.0 [80]. The isotopic ratios and age errors determined during the study are reported at the 1σ level of confidence.

3.5. In Situ Zircon Lu–Hf Isotopic Analyses

After U-Pb dating, zircon grains were newly polished. In situ zircon Lu–Hf isotope analyses were carried out on the same spots or on the same zircon zones where the U–Pb age determinations were made. In situ zircon Lu–Hf isotopes were determined with a 40 μm beam diameter using an Agilent 7700x ICP–MS instrument (Agilent, Santa Clara, CA, USA) coupled to a 193 nm ultraviolet wavelength GeoLas Pro ArF-excimer laser (Coherent, Inc., Santa Clara, CA, USA). Values of 176Lu/175Lu = 0.02669 and 176Yb/172Yb = 0.5886 were applied for the interference corrections of isobars to calculate the 176Lu/77Hf and 176Hf/177Hf values of the analyzed samples [81]. During sample determinations, standard zircons GJ-1 (0.282000 ± 0.000030), MUN (0.282136 ± 0.000030), and Plesovice (0.282482 ± 0.000030) were used for calibration of the sample determinations and instrumental monitoring. The analysis results revealed that the mean values of GJ-1 (0.28199 ± 0.000019), MUN (0.282162 ± 0.000016), and Plesovice (0.282463 ± 0.000014) for the standard samples were the same as the recommended values within error. Calculation of the εHf(t) values employed the present-day chondrite ratios of 176Lu/177Hf = 0.0332 and 176Hf/177Hf = 0.282772, recommended by Francis and Blichert-Toft (1997) [82]. Calculation of the single-stage model ages (TDM1) used the present-day depleted-mantle ratios of 176Hf/177Hf = 0.28325 and 176Lu/177Hf = 0.0384 [83]. The present-day continental upper crust ratio of fLu/Hf = −0.72 and depleted-mantle ratio of fLu/Hf = 0.16 were adopted for the calculation of the two-stage model ages (TDM2) [84].

4. Results

4.1. Whole-Rock Major and Trace Element Contents

Major and trace element contents of the Wushan granitic mylonite and the Yuanlong and Xinyang granitic gneisses are presented in Table 2 and Figures 4 and 5. The granitic mylonite and granitic gneiss samples had high SiO2 (68.03–75.68 wt%), K2O + Na2O (5.64–8.09 wt%), and Al2O3 (12.67–15.64 wt%) contents and low MgO contents (0.11–1.16 wt%) and Mg# values (16–37). The samples are plotted in the granodiorite and granite domains in a total alkalis–silica (TAS) diagram (Figure 4a) and in the high-K calc-alkaline series in a K2O versus SiO2 diagram (Figure 4b). The studied samples yielded aluminum saturation index (A/CNK) values of 1.12 to 1.34 and showed peraluminous characteristics according to an A/CNK–A/NK diagram (Figure 4c). All of these geochemical features indicate that the protoliths of the granitic mylonite and granitic gneiss were potassic peraluminous calc-alkaline granites.

Patterns of chondrite-normalized rare earth element (REE) contents for the nine studied samples are shown in Figure 5a. The samples show enrichment in light REEs (LREEs) and depletion of heavy REEs (HREEs) ((La/Yb) N = 3–10). The Europium anomaly (Eu/Eu*) showed strong negative values of 0.09 to 0.59. In a primitive-mantle-normalized multi-element spider diagram (Figure 5b), the samples exhibited similar trace element patterns, with enrichment in large-ion lithophile elements (LILEs; e.g., Rb, Ba, Th, U, and K) and depletion of high-field-strength elements (HFSEs; e.g., Nb, Ta, and Ti). Two of the granitic gneisses from Xinyang were characterized by low abundances of Sr and Ba (Figure 5b) and large negative Eu anomalies in the chondrite-normalized REE patterns (Figure 5a), which were similar with highly fractionated granite.

Table 2. Whole-rock major and trace element data for the early Neoproterozoic granitic rocks in the western margin of the NQT. [a] A/CNK = $Al_2O_3/(CaO + Na_2O + K_2O)$ molar ratio; A/NK = $Al_2O_3/(Na_2O + K_2O)$ molar ratio; $Mg^{\#}$ = Mg/(Mg+Fe) molar ratio; N = normalization following McDonough and Sun (1995); $Eu/Eu^* = Eu/(Sm_N * Gd_N)^{1/2}$.

Sample	WS20-01	WS20-02	WS20-03	YL20-01	YL20-02	YL20-03	XY20-02	XY20-05	XY20-07
Rock Type	**Granitic Mylonite**			**Granitic Gneiss**					
Major Oxides (%)									
SiO_2	70.42	68.03	69.47	70.53	70.66	71.70	75.68	71.59	75.29
TiO_2	0.49	0.49	0.56	0.50	0.58	0.49	0.13	0.40	0.08
Al_2O_3	14.09	15.64	14.16	14.19	14.00	13.93	12.67	14.09	13.30
TFe_2O_3	3.83	3.75	4.30	3.44	4.41	3.68	1.33	3.36	1.11
MnO	0.07	0.06	0.07	0.07	0.07	0.06	0.03	0.06	0.02
MgO	1.14	0.96	1.16	0.95	1.14	0.92	0.22	0.73	0.11
CaO	2.19	2.45	2.50	1.97	1.24	1.34	0.64	1.51	0.54
Na2O	2.83	3.27	2.65	2.61	2.10	2.08	2.57	2.68	2.87
K2O	3.01	3.82	2.99	3.93	4.36	4.58	5.41	4.19	5.22
P2O5	0.11	0.12	0.11	0.11	0.12	0.09	0.09	0.13	0.19
LOI	1.52	1.27	1.55	1.38	1.25	1.11	1.13	1.26	1.11
TOTAL	99.70	99.86	99.52	99.68	99.93	99.98	99.90	100.00	99.84
A/CNK [a]	1.18	1.12	1.16	1.17	1.34	1.29	1.12	1.20	1.17
A/NK [a]	1.78	1.64	1.86	1.66	1.71	1.66	1.25	1.57	1.28
Na_2O/K_2O	0.94	0.86	0.89	0.66	0.48	0.45	0.48	0.64	0.55
$Na_2O + K_2O$	5.84	7.09	5.64	6.54	6.46	6.66	7.98	6.87	8.09
$Mg^{\#}$	37	34	35	35	34	33	25	30	16
T_{Zr} (°C)	828	836	829	844	867	864	765	828	749

Table 2. *Cont.*

Sample	WS20-01	WS20-02	WS20-03	YL20-01	YL20-02	YL20-03	XY20-02	XY20-05	XY20-07
Rock Type	**Granitic Mylonite**					**Granitic Gneiss**			
Trace Elements (ppm)									
Li	47.6	34.7	40.0	32.7	32.7	42.9	18.9	55.2	71.9
Be	2.83	3.39	3.19	2.58	2.58	2.45	3.28	2.62	2.58
Sc	9.79	10.1	11.0	9.51	9.51	9.58	2.84	6.79	2.78
V	35.7	37.9	41.3	43.2	43.2	43.2	4.33	25.4	1.45
Cr	18.4	19.2	21.8	21.8	21.8	24.4	2.28	12.2	0.88
Co	6.13	5.85	6.87	6.94	6.94	7.46	1.24	5.31	0.32
Ni	7.18	7.30	9.15	10.2	10.2	99.9	1.31	5.51	0.59
Cu	5.73	5.09	8.77	8.30	8.30	16.78	4.99	6.67	1.06
Zn	45.5	54.2	70.2	22.8	22.8	49.5	27.5	84.4	27.7
Ga	18.4	19.2	18.4	18.6	18.6	22.0	13.8	18.3	20.0
Ge	1.52	1.62	1.63	1.67	1.67	1.78	1.62	1.71	2.19
Rb	121	159	155	146	146	196	259	233	430
Sr	126	145	121	156	156	99.4	33.1	106	18.9
Zr	196	198	208	217	217	209	75	163	59.9
Nb	10.9	10.9	11.9	12.7	12.7	11.5	6.69	10.9	10.5
Cs	4.99	12.0	17.9	5.16	5.16	11.9	7.50	18.6	13.4
Ba	593	668	529	799	799	858	299	533	36.9
Hf	5.43	5.50	5.66	5.86	5.86	5.61	2.72	4.64	2.70
Ta	1.01	0.93	0.95	1.03	1.03	0.93	0.94	0.97	1.92
Pb	27.2	36.9	21.1	34.6	34.6	35.6	32.7	14.3	25.3
U	3.71	4.72	5.04	2.94	2.94	3.03	2.16	1.66	3.97
Th	15.7	16.3	17.3	20.4	20.4	20.0	12.3	14.3	11.9
REE (ppm)									
La	31.6	29.5	33.1	43.0	43.0	40.9	13.9	31.4	7.87
Ce	66.5	62.6	70.0	90.7	90.7	83.7	32.9	65.1	17.1
Pr	7.70	7.32	8.16	10.4	10.4	9.83	3.59	7.57	2.08
Nd	28.3	26.6	30.0	39.6	39.6	35.9	13.7	27.7	7.41
Sm	5.85	5.41	6.22	7.76	7.76	7.04	3.97	5.77	2.54
Eu	0.95	0.90	0.99	1.34	1.34	1.30	0.30	0.90	0.08
Gd	5.33	4.78	5.72	6.85	6.85	6.09	4.37	5.20	2.77
Tb	0.83	0.77	0.91	1.00	1.00	0.90	0.90	0.82	0.66
Dy	5.02	4.80	5.52	5.84	5.84	5.27	6.06	4.83	4.11
Ho	0.97	0.97	1.06	1.11	1.11	1.04	1.23	0.91	0.63
Er	2.81	2.98	3.09	3.24	3.24	3.07	3.65	2.62	1.48
Tm	0.41	0.45	0.44	0.46	0.46	0.45	0.55	0.38	0.19
Yb	2.73	3.08	2.86	2.94	2.94	2.89	3.55	2.39	1.10
Lu	0.40	0.46	0.42	0.44	0.44	0.44	0.52	0.35	0.14
Y	27.9	27.2	30.7	33.0	33.0	30.9	38.5	28.2	22.7
Rb/Sr	0.96	1.10	1.27	0.93	0.93	1.97	7.85	2.20	22.7
$(La/Yb)_N$ [a]	8	7	8	10	10	10	3	9	5
Eu/Eu* [a]	0.51	0.53	0.50	0.55	0.43	0.59	0.22	0.49	0.09
Σ_{REE}	187	178	199	248	248	230	128	184	71

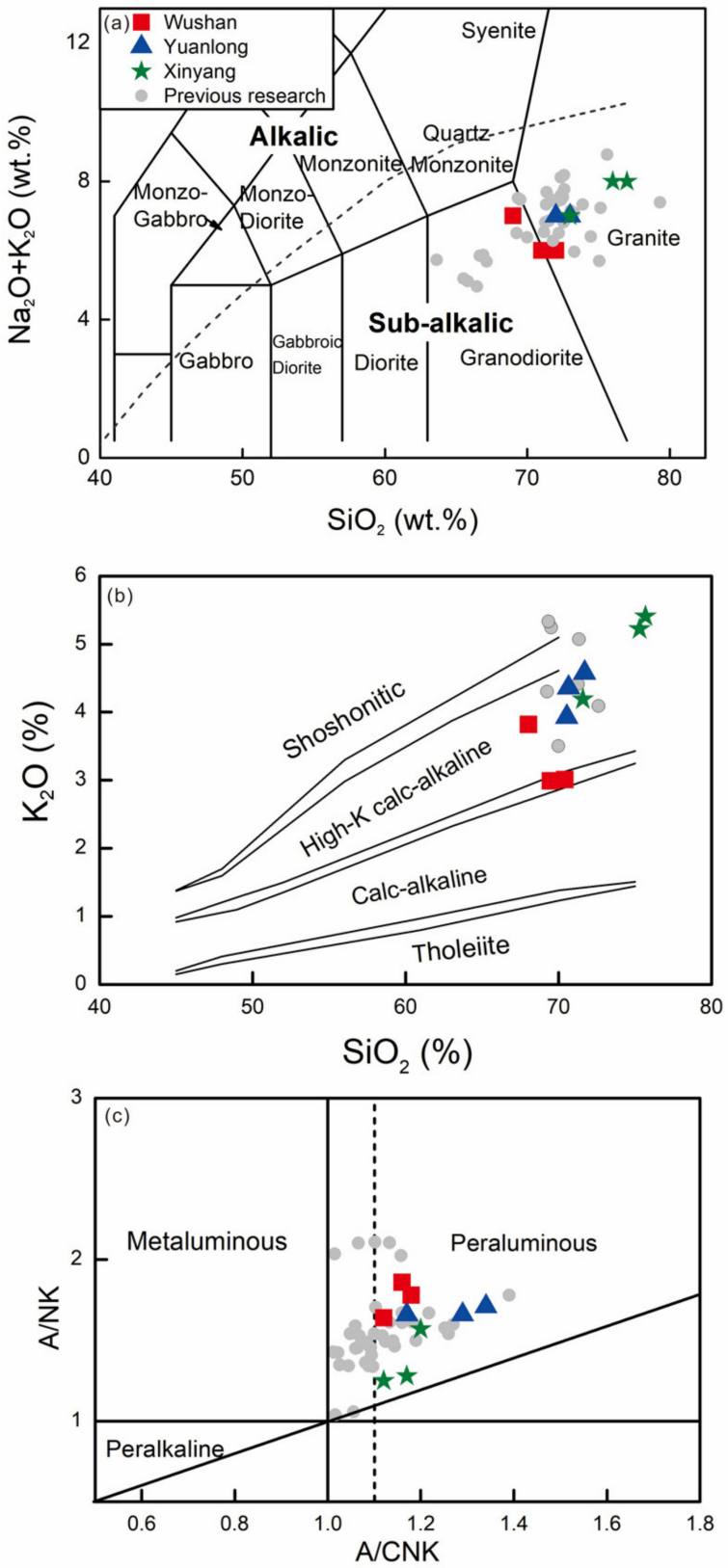

Figure 4. Major element compositions of the studied granitic mylonites and granitic gneisses from the western margin of the NQT: (**a**) total alkalis versus silica (TAS; after [85]) classification diagram; (**b**) K_2O versus SiO_2 classification diagram [86]); (**c**) alumina saturation index diagram [87]. Data sources for the previous research: [19,39–42,52].

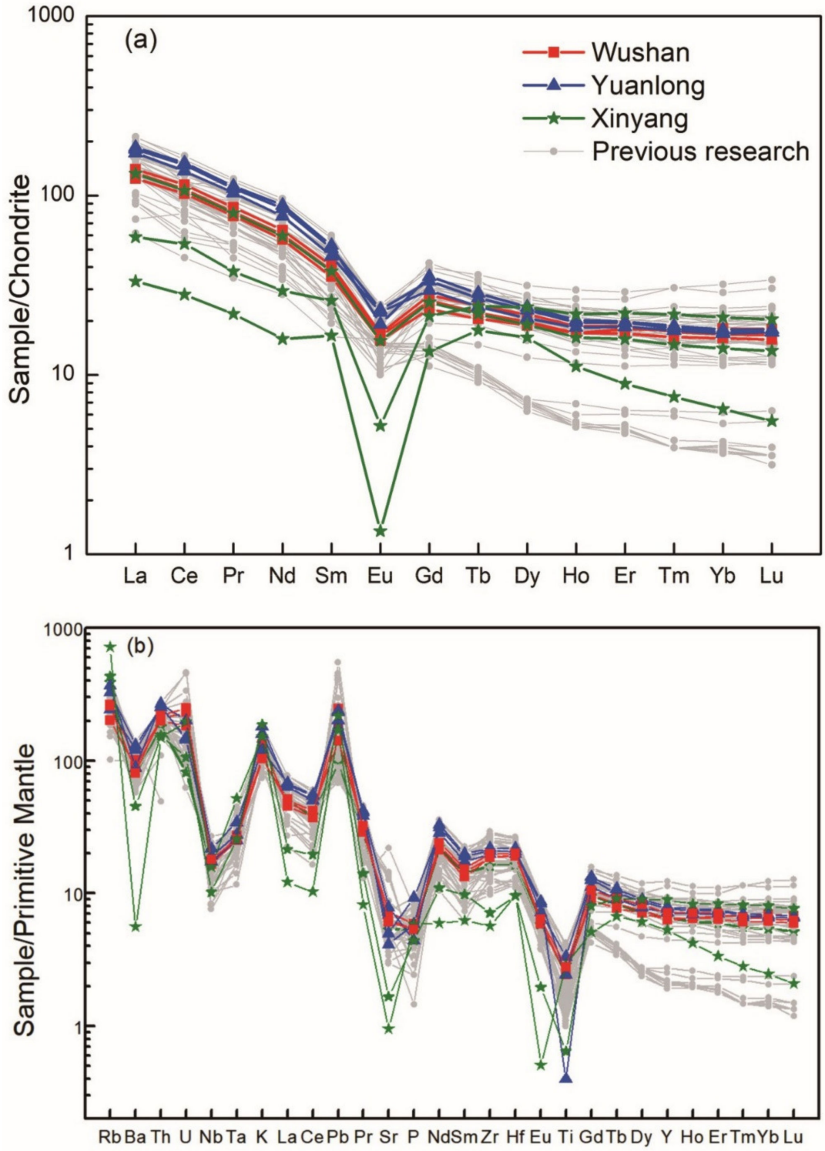

Figure 5. (**a**) Chondrite-normalized REE patterns and (**b**) primitive-mantle-normalized trace element spider diagrams of the studied samples. Data sources for the previous research: [19,39–42,52].

4.2. In Situ Zircon U–Pb Ages, Trace Element Contents, and Lu–Hf and O Isotope Compositions

Here, we present in situ zircon U–Pb–Hf–O isotope compositions and trace element contents for the three granitic mylonite samples (i.e., WS20-01, WS20-02, and WS20-03) from the Wushan area, the three granitic gneiss samples (i.e., YL20-01, YL20-02, and YL20-03) from the Yuanlong area, and the three granitic gneiss samples (i.e., XY20-02, XY20-05, and XY20-07) from the Xinyang area. Representative zircon CL images for the samples are shown in Figure 6. Data for the zircon U–Pb ages, Hf isotopes, O isotopes, and trace elements are given in Tables S1–S4 in the Supplementary Materials, respectively.

Zircon grains from the nine samples were mostly colorless and transparent, subhedral to euhedral, and had lengths of 90–200 μm and aspect ratios of 1:1 to 1:5 (Figure 6). Most of the zircon grains showed oscillatory zoning (Figure 6) and had Th/U ratios higher than 0.1, indicating an igneous origin [88]. A few zircon grains in the samples from Wushan and Xinyang (i.e., WS20-01, WS20-02, WS20-03, and XY20-05) displayed oscillatory zoning bounded by narrow bright metamorphic rims (Figure 6a–c,h). In addition, many zircons from the Xinyang samples had inherited cores (Figure 6g,h).

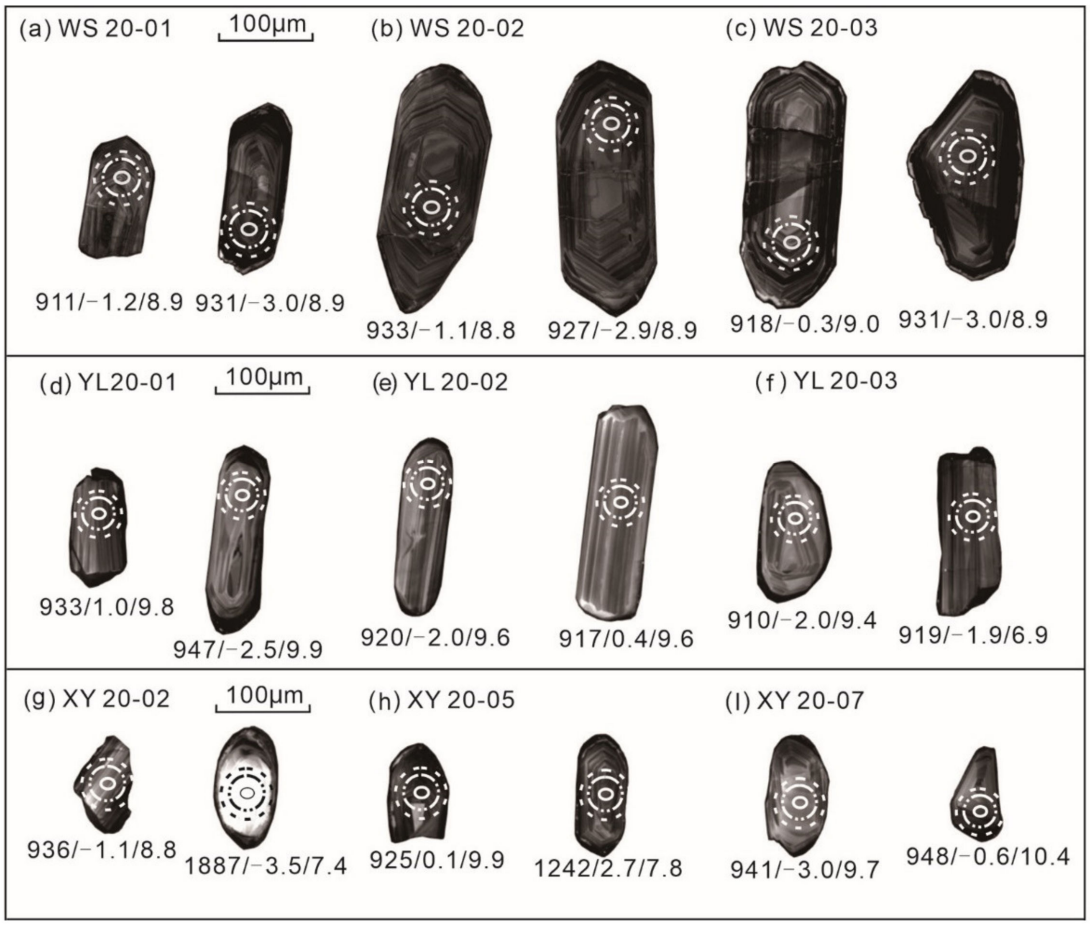

Figure 6. Representative zircon CL images with ages/$\varepsilon_{Hf}(t)$/$\delta^{18}O$ values for the granitic mylonites from Wushan (**a**–**c**) and granitic gneisses from Yuanlong (**d**–**f**) and Xinyang (**g**–**i**) in the western margin of the NQT. The smaller circles 10 μm in diameter, the medium circles 30 μm in diameter, and the dashed circles 40 μm in diameter represent analytical sites for the O, U–Pb, and Lu–Hf isotope determinations, respectively.

4.2.1. Zircon U–Pb Ages

The zircon U–Pb isotopic data of the studied samples are presented in Figure 7. A majority of the zircon analyses yielded concordant ages.

Wushan Granitic Mylonites

Twenty-two analyses of zircons from sample WS20-01 yielded a weighted mean $^{206}Pb/^{238}U$ age of 933 ± 7 Ma (MSWD = 0.8) (Figure 7a). Eighteen analyses of zircons from sample WS20-02 yielded a weighted mean $^{206}Pb/^{238}U$ age of 930 ± 8 Ma (MSWD = 0.7) (Figure 7b). For sample WS20-03, 19 analyzed zircons yielded a weighted mean $^{206}Pb/^{238}U$ age of 927 ± 10 Ma (MSWD = 3.2) (Figure 7c). Data for these three samples gave an overall weighted mean age of 929 ± 5 Ma (MSWD = 6.1), which is interpreted as the crystallization age of the granitic magma from which the Wushan samples were formed.

Yuanlong Granitic Gneisses

A total of 15 analyses were performed for sample YL20-01, yielding a weighted mean $^{206}Pb/^{238}U$ age of 937 ± 8 Ma (MSWD = 0.5) (Figure 7d). Nineteen analyses of zircons from sample YL20-02 gave a weighted mean $^{206}Pb/^{238}U$ age of 924 ± 9 Ma (MSWD = 1.4) (Figure 7e). Nineteen analyses of zircons from sample YL20-03 yielded a weighted mean $^{206}Pb/^{238}U$ age of 935 ± 7 Ma (MSWD = 0.8) (Figure 7f). The three samples gave an overall

weighted mean age of 931 ± 4 Ma (MSWD = 1.0), which is interpreted as the crystallization age of the granitic magma from which the Yuanlong samples were formed.

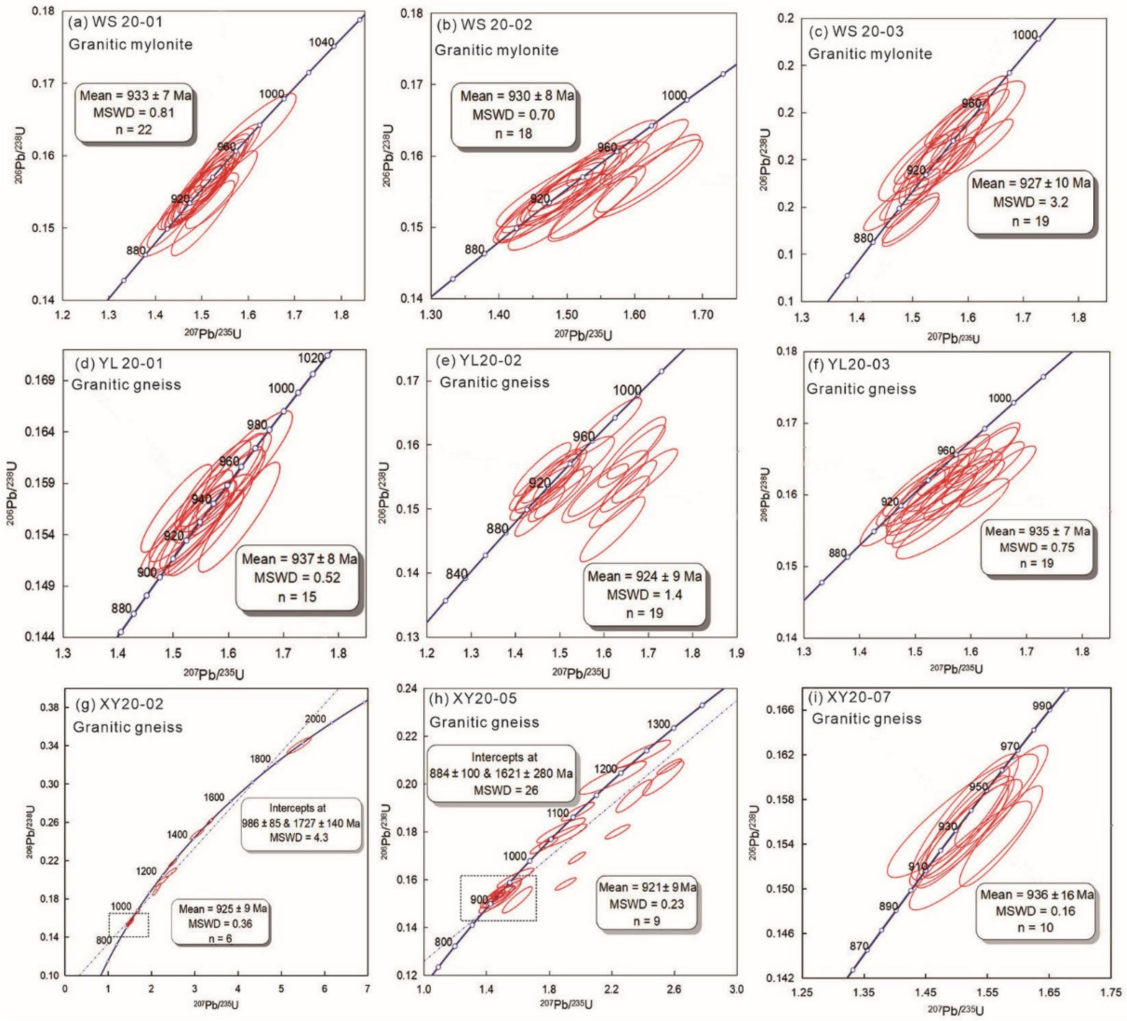

Figure 7. LA–ICP–MS zircon U–Pb concordia diagrams for the granitic mylonites from Wushan (**a**–**c**) and granitic gneisses from Yuanlong (**d**–**f**) and Xinyang (**g**–**i**) in the western margin of the NQT.

Xinyang Granitic Gneisses

Fifteen analyses of cores and rims of zircons from sample XY20-02 defined a discordia line with an upper intercept at 1727 ± 140 Ma and a lower intercept at 986 ± 85 Ma (MSWD = 4.3) (Figure 7g). Seven analyses of magmatic zircon rims gave a weighted mean $^{206}Pb/^{238}U$ age of 925 ± 9 Ma (MSWD = 0.36) (Figure 7g), close to the lower intercept of the concordia diagram and likely representing the protolith age of the granitic gneiss. The remaining eight inherited cores yielded four older concordant ages (i.e., 1887, 1497, 1425, and 1280 Ma) and four discordant analyses. Twenty-three analyses of zircons from sample XY20-05 plotted a discordia line with an upper intercept at 1621 ± 280 Ma and a lower intercept at 884 ± 100 Ma (MSWD = 26; Figure 7h). Nine analyses of magmatic zircon rims gave a weighted mean age of 921 ± 9 Ma (MSWD = 0.23) (Figure 7h). The remaining analyses included 4 older concordant ages (i.e., 1244, 1111, 1070, and 1035 Ma) and 10 discordant ages. Ten analyses of zircons from sample XY20-07 yielded a weighted mean $^{206}Pb/^{238}U$ age of 936 ± 16 Ma (MSWD = 0.16) (Figure 7i). The three samples gave an overall weighted mean age of 931 ± 7 Ma (MSWD = 2.3), which is interpreted as the crystallization age of the granitic magma from which the Xinyang samples were formed.

4.2.2. Zircon Trace Elements

Zircon trace element contents were obtained from the same analytical spots from where the zircon U–Pb data were acquired. The detailed analysis results for zircon trace elements are presented in Table S2. Chondrite-normalized REE patterns for the zircons are shown in Figure 8. Most of the analyzed zircon grains displayed enrichment in HREEs and depletion of LREEs ((La/Yb)N < 0.031), and they showed positive Ce anomalies (Ce/Ce* = 1.1–137) and negative Eu anomalies (Eu/Eu* = 0.00–0.58), similar to the characteristics of typical magmatic zircons (Corfu et al., 2003; Hoskin and Black, 2010). The presence of accessory mineral inclusions, such as apatite or titanite, can explain the LREE enrichment of some zircon grains [89,90].

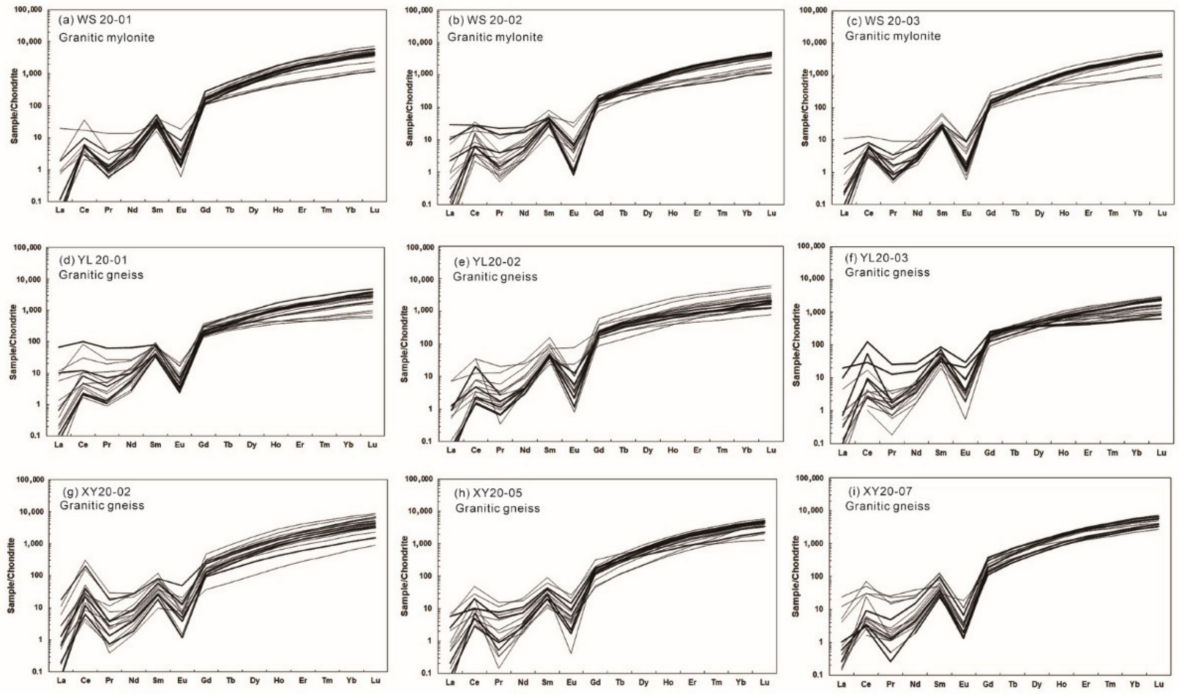

Figure 8. Chondrite-normalized REE patterns for zircons from the granitic mylonites from Wushan (**a**–**c**) and granitic gneisses from Yuanlong (**d**–**f**) and Xinyang (**g**–**i**) in the western margin of the NQT.

4.2.3. Zircon Lu–Hf Isotopes

Zircon Lu–Hf isotope data of the granitic mylonites and granitic gneisses are presented in Table S3 and Figure 9.

Wushan Granitic Mylonite

The magmatic zircon grains of the three analyzed granitic mylonite samples showed a range in initial $^{176}Hf/^{177}Hf$ from 0.281935 to 0.282289 and $\varepsilon_{Hf}(t)$ values from −9.2 to 2.1, with a weighted mean $\varepsilon_{Hf}(t)$ value of -1.5 ± 0.4 (MSWD = 7.1) (Table S3 and Figure 9a). The calculated T_{DM2} ages ranged from 2.10 to 1.53 Ga, with a weighted mean T_{DM2} age of 1.70 Ga (Table S3 and Figure 9d).

Yuanlong Granitic Gneiss

The magmatic zircon grains from the Yuanlong granitic gneiss had $^{176}Hf/^{177}Hf$ values of 0.281874 to 0.282254 and corresponding $\varepsilon_{Hf}(t)$ values of −10.6 to 1.2, with a weighted mean $\varepsilon_{Hf}(t)$ value of -2.0 ± 0.5 (MSWD = 9.6) (Table S3 and Figure 9b). The calculated T_{DM2} ages ranged from 2.19 to 1.56 Ga, with a weighted mean T_{DM2} age of 1.73 Ga (Table S3 and Figure 9e).

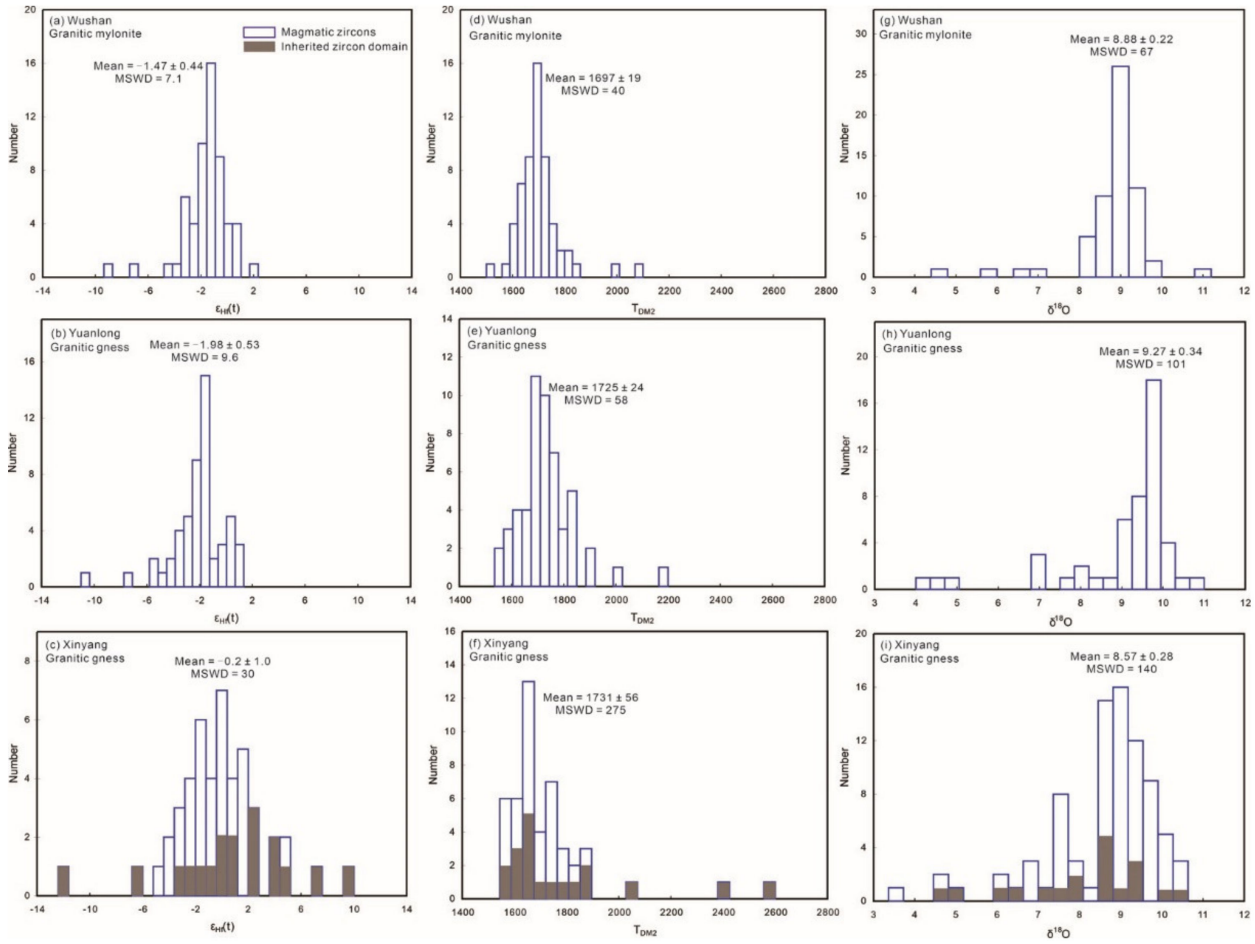

Figure 9. Histograms of the $\varepsilon_{Hf}(t)$, T_{DM2}, and $\delta^{18}O$ values of zircons from the granitic mylonites from Wushan (**a**–**c**) and granitic gneisses from Yuanlong (**d**–**f**) and Xinyang (**g**–**i**) in the western margin of the NQT.

Xinyang Granitic Gneiss

The magmatic zircons from the three samples of the Xinyang granitic gneiss had $^{176}Hf/^{177}Hf$ values of 0.282042 to 0.282285 and corresponding $\varepsilon_{Hf}(t)$ values from −4.9 to 1.6, with a weighted mean $\varepsilon_{Hf}(t)$ value of −0.2 ± 1.0 (MSWD = 30). The calculated T_{DM2} ages ranged from 1.89 to 1.55 Ga, with a weighted mean T_{DM2} age of 1.73 Ga (Table S3 and Figure 9f). The core domains of the inherited zircons showed a wide range in initial $^{176}Hf/^{177}Hf$ values from 0.281501 and 0.282244 and $\varepsilon_{Hf}(t)$ values ranging from −12.2 to 9.7 (Table S3). The calculated T_{DM2} ages ranged from 2.57 to 1.57 Ga (Table S3).

4.2.4. Zircon O Isotopes

Zircon O isotope data from the nine studied samples are given in Table S4. The $\delta^{18}O$ values calculated from the experimental data are presented in Figure 9g–i.

Magmatic zircons from the nine samples showed a wide range of $\delta^{18}O$ values (3.56‰ to 11.07‰) (Figure 9g-i). The weighted mean zircon $\delta^{18}O$ values were calculated as 8.88‰ ± 0.22‰ (MSWD = 67) for the Wushan granitic mylonite, 9.27‰ ± 0.34‰ (MSWD = 101) for the Yuanlong granitic gneiss, and 8.57‰ ± 0.28‰ (MSWD = 140) for the Xinyang granitic gneiss.

5. Discussion

5.1. Age of Granitic Magmatism

Numerous studies have investigated the petrogenesis and tectonic setting of Neoproterozoic granitic rocks in the eastern part of the NQT. Early Neoproterozoic granitic gneisses from the region have yielded zircon U–Pb ages ranging from 980 to 880 Ma [19,30,34,37,39–42,51,52]. In the present study, new zircon U–Pb LA–ICP–MS data for granitic mylonites and granitic gneisses from the western margin of the NQT yielded early Neoproterozoic ages ranging from 936 to 921 Ma. These ages confirm that Precambrian granitic rocks of the QOB are not restricted to the eastern part of the NQT.

A comparison of our new ages with the published data of early Neoproterozoic granitic rocks from the NQT is presented in Figure 10. The protolith ages of the granitic mylonite and granitic gneiss lie between 1000 and 880 Ma, with a peak at ca. 930 Ma [19,31,36,40,41]. In addition, syenites and syenogranites from the Fangcheng area yielded crystallization ages of 874 to 843 Ma [18,51].

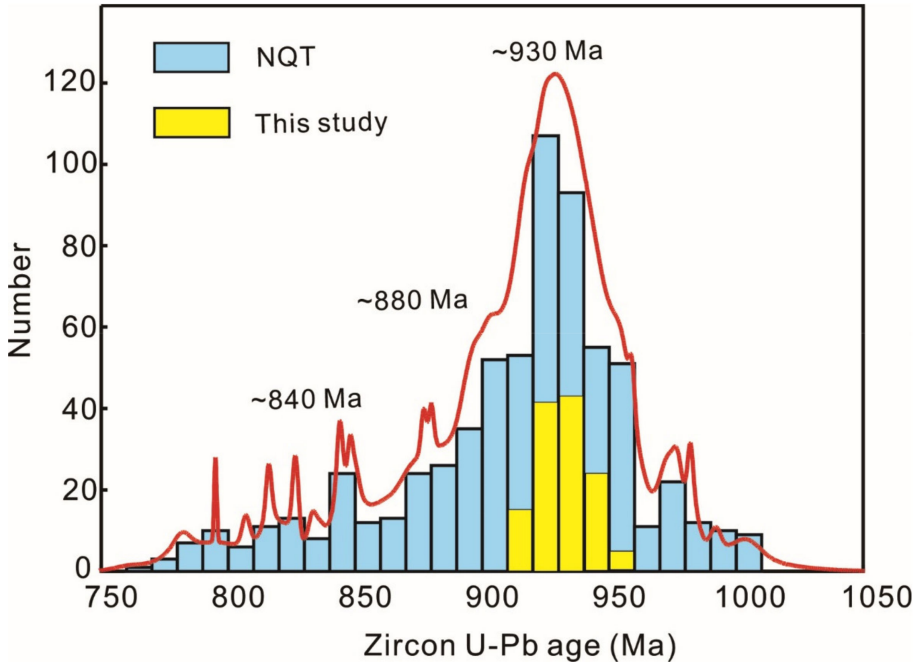

Figure 10. U–Pb zircon age histogram with a probability density plot for Neoproterozoic granitic rocks from the NQT. Data sources for the eastern part of the NQT: [18–20,30,32–34,36,37,39–42,51,52].

As inherited zircon cores represent restite of granitic rock sources in the deep continental crust, their ages are important for determining the nature of the sources. The large contribution (Figure 7g,h) of Paleo- to Mesoproterozoic (ca. 1.9–1.0 Ga) inherited zircon ages identified in the Xinyang granitic gneiss samples indicates that their protoliths were derived from Paleo- to Mesoproterozoic basement.

5.2. Nature of the Magma Source

Peraluminous granites constitute part of the orogenic belts and are formed through the anatexis of supracrustal rocks [4–7,9] and of sedimentary rocks in particular [4,91]. However, various studies have demonstrated that the source of peraluminous granites is complex. Such granites can be derived from either pelite [92] or sandstone or greywacke [93,94]). Meta-igneous rocks have also been reported as a possible source of peraluminous granite [95,96].

The granitic mylonites and granitic gneisses from the Tianshui area of the western margin of the NQT showed similar major and trace element contents and zircon U–Pb–Hf–O isotopic compositions, indicating that the magma that formed these rocks was derived

from the same source. The Hf–O isotopic compositions of zircon can be used to trace the source of granitic magma, whether derived from reworked crust, juvenile crust, or mantle-derived materials (Hawkesworth and Kemp, 2006; Kemp et al., 2010). The studied granitic mylonites and granitic gneisses from the Tianshui area showed high SiO_2 (68.03–75.68 wt%) and low MgO (0.11–1.16 wt%) and Mg# (16–37). Most of the analyzed zircons were higher than the O isotope value of normal mantle (5.3‰ ± 0.6‰ (2σ); [97]. The high $\delta^{18}O$ values and lack of relationship between the Hf and O isotopic compositions (Figure 11a) suggest that they were derived from heterogeneous crustal rocks rather than magma mixing [98].

We compiled previously published Hf–O isotope data (from the areas of Zhaigen, Fangzhuang, and Dehe) [41] for the eastern part of the NQT and compared them with our data to constrain the source of Neoproterozoic granitic magmatism in the QOB (Figure 11). Magmatic zircons from the studied granitic rocks had similar protolith ages (936–921 Ma; Figure 7), Hf isotopic compositions ($\varepsilon_{Hf}(t)$ = −10.6 to 2.1), and T_{DM2} ages (2.20 to 1.53 Ga) to published data for early Neoproterozoic granitic rocks from the eastern part of the NQT (Table S3 and Figure 11b). The wide range of $\varepsilon_{Hf}(t)$ values and T_{DM2} ages suggests that the early Neoproterozoic granitic magma of the QOB was derived from reworked Paleoproterozoic crust (2.2 to 1.6 Ga) and Mesoproterozoic juvenile crust (1.6 to 1.5 Ga) (Figure 11b).

The Hf isotopic composition from the core domains of inherited zircons is crucial in determining the composition of the source. The core domains of inherited zircons identified from the Xinyang samples showed a wide range in $\varepsilon_{Hf}(t)$ values from −12.2 to 9.7 and calculated T_{DM2} ages of 2.57 to 1.57 Ga (Table S3). We compared our data with a compilation of Hf isotopic data for detrital zircons from the Qinling Group [99,100] (Figure 11b,c). Most of the magmatic zircons and core domains of inherited zircons fell in the range of the Qinling Group (Figure 11b,c), implying that the Qinling Group was an important source for the studied early Neoproterozoic granitic rocks.

Zircon $\delta^{18}O$ values can help to establish whether granitic magma originated directly from the mantle or was influenced by the involvement of supracrustal material [101,102]. Most of the analyzed zircons showed high $\delta^{18}O$ values (Figures 9g–i and 11a and Table S4) that were similar to published data for early Neoproterozoic granitic rocks from the areas of Zhaigen, Fangcheng, and Dehe in the eastern part of the NQT (Figure 11a). Moreover, these zircons showed a wide range of $\varepsilon_{Hf}(t)$ values (−12.2 to 13.6; Figure 11a). High $\delta^{18}O$ and wide-ranging $\varepsilon_{Hf}(t)$ values are generally interpreted as indicating the involvement of intensely weathered sedimentary rocks in the magma source [97]. However, seven zircons from samples WS20-01, YL20-01, YL20-02, XY20-02, and XY20-05 had lower $\delta^{18}O$ values of 3.56‰ to 4.73‰ and a restricted range of $\varepsilon_{Hf}(t)$ values (Figure 11a; −5.2 to 1.6), indicating the involvement of igneous rocks that had been subjected to high-temperature water–rock interaction [103,104]. The Hf–O isotopic compositions of the analyzed zircons indicate that the early Neoproterozoic granitic magma was derived from two crustal sources: predominant supracrustal sedimentary rocks and subordinate igneous rocks.

The source materials for the strongly peraluminous granitic rocks can be distinguished by the CaO/Na_2O ratio [105]. Apart from two samples from the Xinyang area, data for the studied granitic rocks and previous data from the NQT show CaO/Na_2O ratios of >0.3. These data indicate that the source materials of early Neoproterozoic granitic rocks in the NQT was predominantly of supracrustal psammite (Figure 11d).

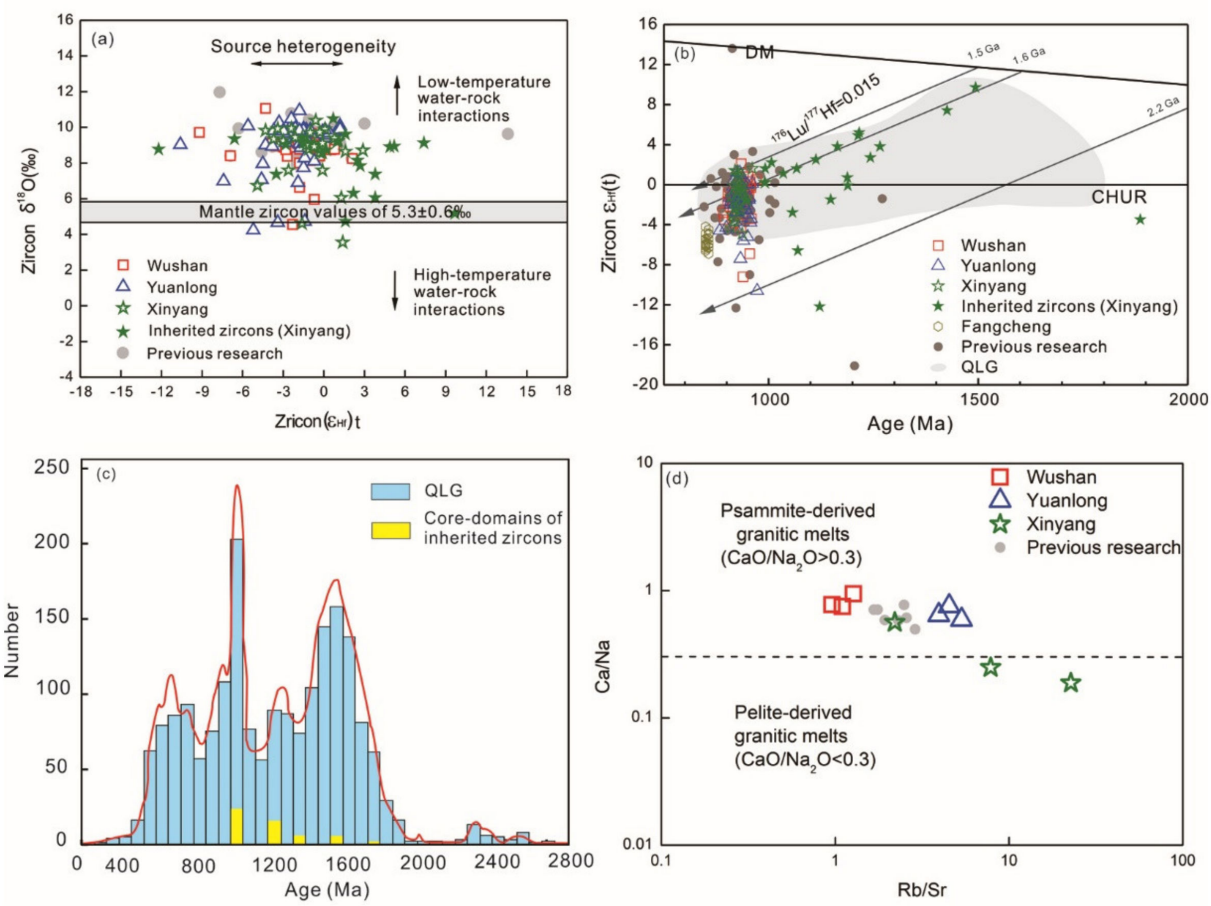

Figure 11. (**a**) Plot of $\delta^{18}O$ versus $\varepsilon_{Hf}(t)$ for zircons from Neoproterozoic granitic rocks from the QOB. The data source for the previous research: [41]. (**b**) Plot of $\varepsilon_{Hf}(t)$ versus U–Pb age for zircons from the studied Neoproterozoic granitic mylonites from Wushan and granitic gneisses from Yuanlong and Xinyang in the western margin of the NQT as well as gneisses from the Qinling Group (QLG) in the NQT. Data sources: Fangcheng [51]; previous research for the biotite monzonitic gneiss and granites from Fangzhuang, Zhaigen, and Dehe [20,41] and the QLG [99,100]. (**c**) U–Pb zircon age histogram with a probability density plot for the QLG and comparison with ages from the core domains of inherited zircons of this study. Data sources for the QLG: [99,100,106–109]. (**d**) Ca/Na–Rb/Sr diagram [105] for the studied granitic mylonites from Wushan and granitic gneisses from Yuanlong and Xinyang. Data sources for the previous research: [19,39–42,52].

5.3. Petrogenesis

Original magmatic compositions are potentially influenced by the metamorphism and alteration. Therefore, the element mobility should be evaluated prior to any petrogenetic discussions. Firstly, all samples possessed loss on ignition (LOI) values of less than 1.6 wt% (Table 2), inconsistent with the strong hydration in these rocks during metamorphism and alteration. Some major elements (e.g., Na and K) and large ion lithophile elements (e.g., Rb and Ba) were regarded to be mobile during post-magmatic metamorphism and alteration [110]. Nevertheless, most samples had coherent patterns in the chondrite-normalized REE diagram and the primitive-mantle-normalized spider diagram (Figure 5), confirming the preservation of the original signatures. Previous studies demonstrated that REE and transition metals are relatively immobile during greenschist-to amphibolite-facies metamorphism and alterations [111–113]. Therefore, the REE and HFSE (i.e., Th, Nb, Ta, Zr, and Hf) compositions of our samples were not affected by the regional greenschist-to amphibolite-facies metamorphism and alteration and essentially reflect the original magmatic compositions.

Although the magma source is considered to be the primary control on the geochemical composition of granitic rocks [114]), rock composition can also be influenced by magmatic processes such as partial melting, magma mixing, and fractional crystallization [115]. Previous studies have demonstrated that strongly peraluminous granitoids can be derived by mixing of mantle- and crust-derived melts [103,116–118]. However, as discussed above, the magma mixing model is unsuitable for explaining the genesis of the Tianshui granitic rocks.

Data of the Tianshui granitic rocks exhibited a trend of fractional crystallization in an La/Sm–Sm diagram (Figure 12a). The major elements of Fe_2O_3 and TiO_2 showed negative relationships with Zr in Harker diagrams (Figure 12d,g), which suggests that crystal fractionation involved Ti–Fe-oxides. Although the samples showed strong negative Eu anomalies in chondrite-normalized REE patterns (Figure 5b), a weak relationship was observed between Eu/Eu* and Zr in Harker diagrams (Figure 12f), indicating that fractional crystallization of plagioclase was minor during magmatic evolution.

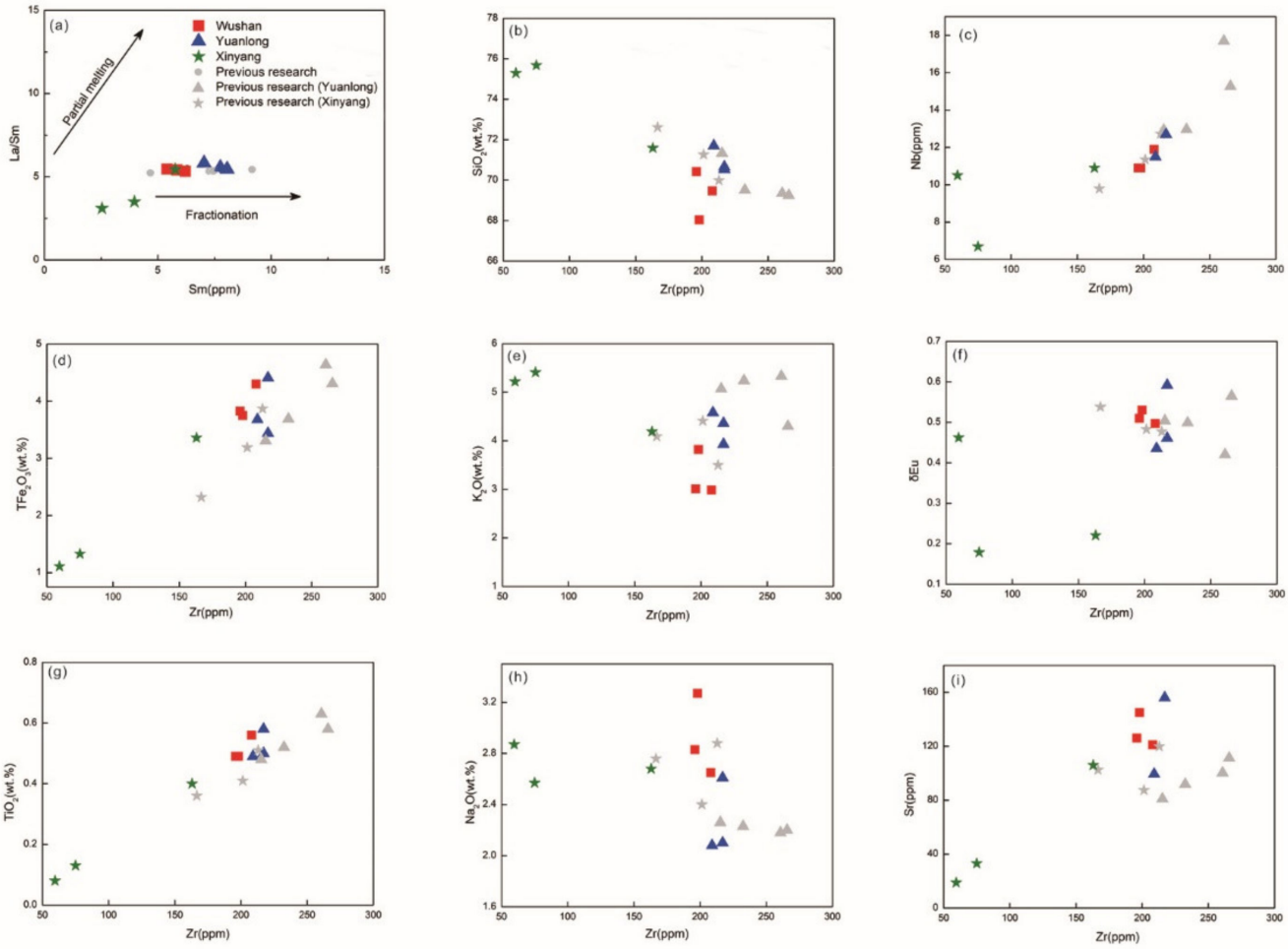

Figure 12. (**a**) La/Sm–Sm diagram illustrating trends in the partial melting and fractional crystallization of the studied granitic rocks from the western margin of the NQT. Harker diagrams (**b**–**i**) for major and selected trace elements for the studied samples. Data source for the previous research: [52].

The geochemical composition of the granitic rocks is also affected by the melting conditions such as water content, temperature, and pressure [94,119]. Dehydration melting occurs through the breakdown of hydrous minerals [120], whereas hydration melting proceeds via the flux of free water into the lithological system [121–123]. The studied granitic mylonites and granitic gneisses showed high K_2O contents (2.99–5.41 wt%) and Rb/Sr ratios (0.93–22.7), low Na_2O/K_2O ratios (0.45–0.94), and negative Eu anomalies, similar to the values expected from melt produced by dehydration melting [123].

The temperature of the primary magma can be estimated based on zircon saturation thermometry [124] and Ti-in-zircon thermometry [125–127]. Calculated T_{Zr} (temperature of zircon saturation) values for the studied granitic rocks were between 749 and 867 °C (mean = 823 °C) (Table 2). Schiller and Finger (2019) [128] proposed that a constant temperature correction by adding 70 °C to the calculated Ti-in-zircon temperatures can give reliable results for ilmenite-bearing granites (that is, almost all S-type and many I-type granites). According to this method, the calculated Ti-in-zircon temperatures for the studied granitic rocks ranged from 700 to 1390 °C (mean = 825 °C) (Figure 13a; [127,128]. The results for the zircon saturation and Ti-in-zircon thermometric methods gave a consistent temperature of ca. 825 °C, corresponding to the temperature for "hot granites" [129]. In addition, Miller et al. (2003) [129] suggested that the T_{Zr} values of granites that contain abundant inherited zircons represent the upper temperature limit of the magma. Therefore, our calculated T_{Zr} for the Xinyang samples, which contained numerous inherited zircons, represents a maximum magma temperature of 825 °C.

The Tianshui granitic rocks showed strong negative Eu anomalies in chondrite-normalized REE patterns, indicating that plagioclase was an important residual phase. Numerous experimental studies have shown that plagioclase dominates residues at pressures of <1.0 GPa (depth < 30 km) [130–132]. Stevens et al. (1997) [133] conducted experiments of biotite dehydration melting of metapelites and metagreywackes at 0.5 GPa in a temperature range of 750 to 830 °C and produced peraluminous leucogranites in equilibrium with granulite-facies residual mineral assemblages. Combining these previous results with the magma temperature calculated in the present study (825 °C), we infer that the Tianshui granitic magma was generated by biotite dehydration melting [123,134].

In summary, the early Neoproterozoic granitic rocks from the western margin of the NQT were most likely derived from biotite dehydration melting of heterogeneous sources at lower crustal depths.

5.4. Tectonic Implications

The Wushan, Yuanlong, and Xinyang granitic mylonites and granitic gneisses contained aluminum-rich minerals of muscovite and garnet and had high A/CNK values of 1.12 to 1.34. These characteristics suggest that their protolith was peraluminous granite. Early Neoproterozoic peraluminous granites have also been identified in the eastern part of the NQT and AQKNQ [20,27,31,37,38,55–57,60,61,136]). The combined zircon U–Pb–Hf–O isotopic compositions of the early Neoproterozoic peraluminous granites from the QOB (Figures 10 and 11) confirmed that these rocks were derived predominantly from the partial melting of supracrustal sedimentary rocks.

Peraluminous granites are generally considered to form in syn-collisional settings [135,137,138]. Early Neoproterozoic peraluminous granites in the eastern part of the NQT and AQKNQ are thought to have formed during syn-collisional processes associated with the assembly of the Rodinia supercontinent [20,27,31,37,38,55–57,60,61,136]. Similarities in age and tectonic setting suggest a correlation of Neoproterozoic granitic magmatism between the NQT and AQKNQ. This correlation implies NQT and AQKNQ might be within a single tectonic domain in the early Neoproterozoic. Moreover, all of the Neoproterozoic peraluminous granites of the NQT fell in the syn-collision and island arc fields in an Nb versus Y tectonic discrimination diagram (Figure 13b; [135]), further indicating that the granitic rocks from the NQT were also formed in a syn-collisional setting. On the basis of our new results and those of previous studies, we propose a genetic model for the early Neoproterozoic peraluminous granites of the NQT (Figure 14a). In this model, the early Neoproterozoic peraluminous granites were formed by partial melting of predominant subducted supracrustal sedimentary rocks and subordinate igneous rocks at lower crustal depths during the syn-collision at 936–921 Ma.

Neoproterozoic alkaline rocks (ca. 874-843 Ma) have been reported from the Fangcheng area in the eastern part of the NQT and are considered to have been emplaced in a post-collisional extensional regime [18,51]. In addition, the early Neoproterozoic mafic rocks

were emplaced at 840~750 Ma [68,70,71] Diwu and Long (2018) [139], also suggesting that these rocks were formed in an extensional setting related to the breakup of the Rodinia supercontinent.

During ca. 936-843 Ma, the syn-collisional (Figure 14a; 936–921 Ma) to post-collisional extensional setting (Figure 14b; at least ca. 874 Ma) resulted in the development of numerous early Neoproterozoic granitic and mafic intrusions in the QOB, in response to the assembly and breakup of the Rodinia supercontinent.

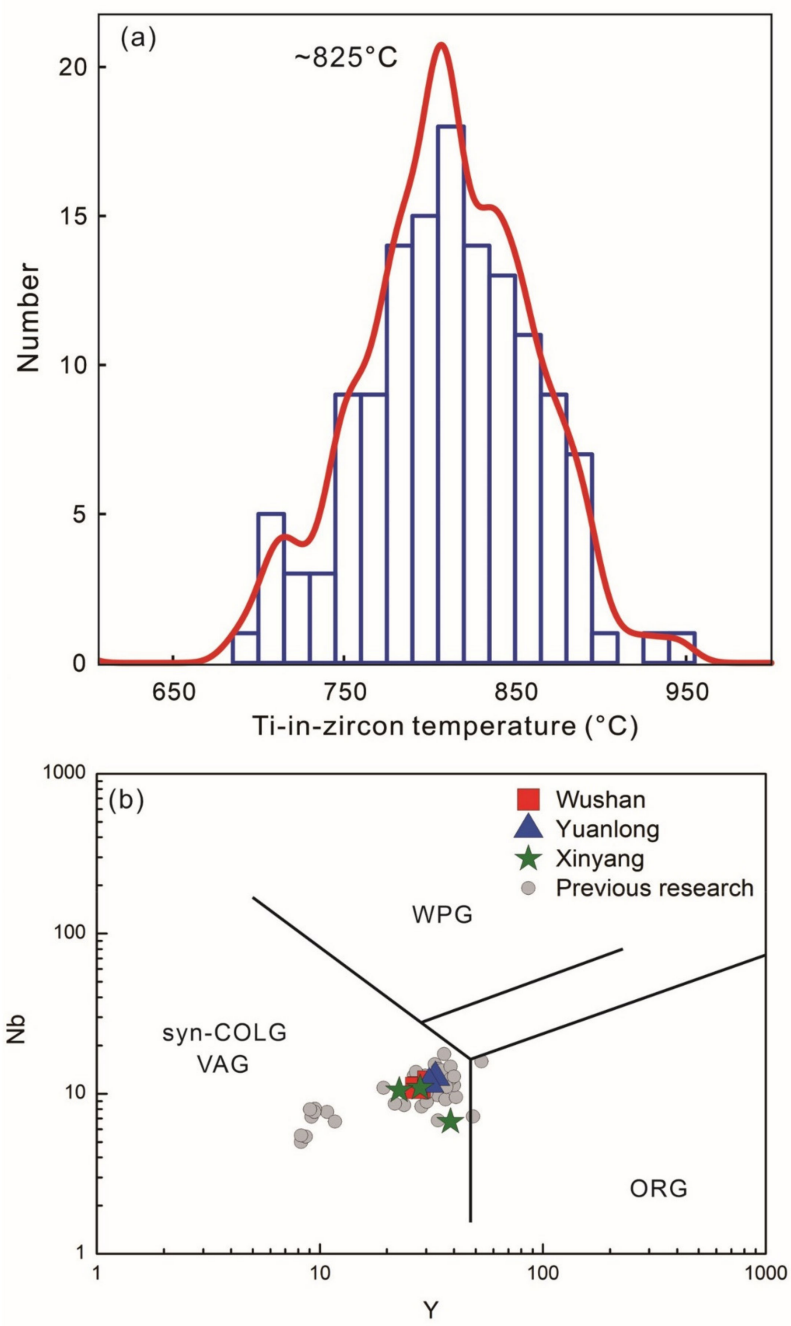

Figure 13. (**a**) Ti-in-zircon temperature [127] histogram with probability density plot for the studied granitic mylonites and granitic gneisses from the western margin of the NQT. (**b**) Nb–Y diagram [135] for the studied granitic mylonites from Wushan and granitic gneisses from Yuanlong and Xinyang. Data sources for the previous research: [19,39–42,52]. VAG—volcanic arc granites; ORG—ocean ridge granites; WPG—within plate granites; Syn-COLG—syn-collision granites.

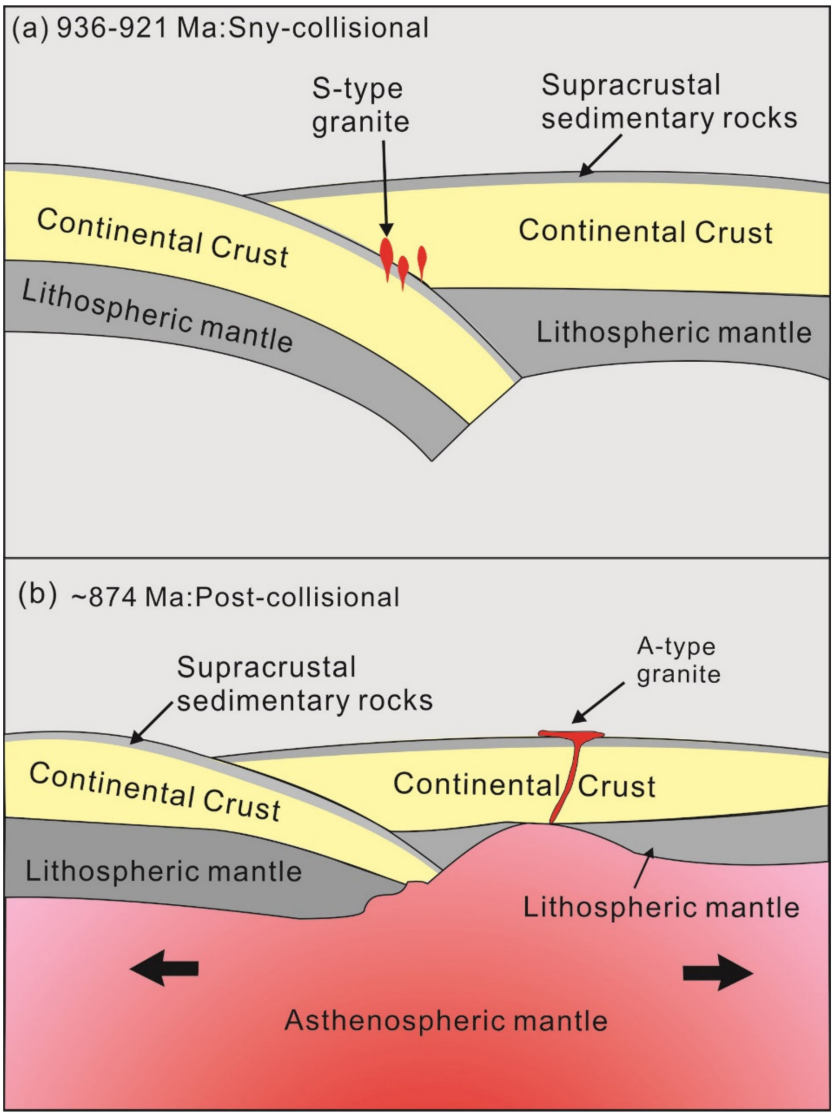

Figure 14. (**a**) Schematic illustrations showing the tectonic evolution of the NQT during the Sny-collisional environment in the early Neoproterozoic. (**b**) Schematic illustrations showing the tectonic evolution of the NQT during the Post-collisional environment in the early Neoproterozoic.

6. Conclusions

We investigated Neoproterozoic peraluminous granitic rocks from the Tianshui area, western margin of the NQT, China, using whole-rock geochemistry and zircon trace elements and U–Pb–Hf–O isotopes to determine their source nature, petrogenesis, and tectonic setting. Our main conclusions are as follows.

(1) The early Neoproterozoic peraluminous granitic rocks from the western margin of the NQT were formed at 936–921 Ma. The ages from the core domains of inherited zircons indicated that the protolith of the granitic rocks was derived from Paleo- to Mesoproterozoic basement;

(2) The early Neoproterozoic peraluminous granitic rocks were derived from reworked Paleoproterozoic crust (2.2 to 1.6 Ga) and Mesoproterozoic juvenile crust (1.6 to 1.5 Ga). The early Neoproterozoic granitic magma is inferred to have been derived from two crustal sources: predominant supracrustal sedimentary rocks and subordinate igneous rocks;

(3) The early Neoproterozoic peraluminous granitic rocks were formed by biotite dehydration melting at lower crustal depths, involving the anatexis of subducted crustal materials in a syn-collisional setting.

Supplementary Materials: The following supporting information can be downloaded at: https://www.mdpi.com/article/10.3390/min12070910/s1, Table S1: LA-ICPMS zircon U-Pb isotope data for the early Neoproterozoic granitic rocks in the western margin of the NQT [127]; Table S2: Zircon trace element concentrations for the early Neoproterozoic granitic rocks in the western margin of the NQT; Table S3: LA-MCICPMS zircon Lu-Hf isotope data for the early Neoproterozoic granitic rocks in the western margin of the NQT [84]; Table S4: SIMS zircon O isotope data for the early Neoproterozoic granitic rocks in the western margin of the NQT.

Author Contributions: Methodology, Z.B.; investigation, A.L.; writing—original draft preparation, G.Y.; writing—review and editing, J.Z. and H.Z. All authors have read and agreed to the published version of the manuscript.

Funding: This study was supported by the National Natural Science Foundation of China (41688103) and the Science and Technology Plan Project of Shaanxi Province, China (2019JCW-19).

Data Availability Statement: Data supporting the reported results are available in this article and in supplementary materials.

Acknowledgments: We thank Mengqi Jin and Yanguang Li for their help with Hf isotopic analyses, Jianqi Wang and Ye Liu for their help with major and trace element analysis, and Xiaoping Xia and Zexian Cui for their help with SIMS zircon O isotope analysis.

Conflicts of Interest: The authors declare no conflict of interest.

References

1. Cawood, P.A.; Kröner, A.; Collins, W.J.; Kusky, T.M.; Mooney, W.D.; Windley, B.F. Accretionary orogens through Earth history. *Geol. Soc.* **2009**, *318*, 1–36. [CrossRef]
2. Kröner, A.; Kovach, V.; Belousova, E.; Hegner, E.; Armstrong, R.; Dolgopolova, A.; Seltmann, R.; Alexeiev, D.V.; Hoffmann, J.E.; Wong, J. Reassessment of continental growth during the accretionary history of the Central Asian Orogenic Belt. *Gondwana Res.* **2007**, *25*, 103–125. [CrossRef]
3. Moyen, J.F.; Laurent, O.; Chelle-Michou, C.; Couzinié, S.; Vanderhaeghe, O.; Zeh, A.; Villaros, A.; Gardien, V. Collision vs. subduction-related magmatism: Two contrasting ways of granite formation and implications for crustal growth. *Lithos* **2017**, *277*, 154–177. [CrossRef]
4. Chappell, B.W.; White, A.J.R. Two contrasting granite types. *Pac. Geol.* **1974**, *8*, 173–174.
5. Chappell, B.W.; White, A.J.R. I- and S-type granites in the Lachlan Fold Belt. *Earth Environ. Sci. Trans. R. Soc. Edinb.* **1992**, *83*, 1–26.
6. Chappell, B.W.; White, A.J.R. Two contrasting granite types: 25 years later. *Aust. J. Earth Sci.* **2001**, *48*, 489–499. [CrossRef]
7. Clemens, J.D. S-type granitic magmas-petrogenetic issues, models and evidence. *Earth-Sci. Rev.* **2003**, *61*, 1–18. [CrossRef]
8. Chen, Y.X.; Song, S.G.; Niu, Y.L.; Wei, C.J. Melting of continental crust during subduction initiation: A case study from the Chaidanuo peraluminous granite in the North Qilian suture zone. *Geochim. Cosmochim. Acta* **2014**, *132*, 311–336. [CrossRef]
9. Zhu, Z.Y.; Campbell, I.H.; Allen, C.M.; Burnham, A.D. S-type granites: Their origin and distribution through time as determined from detrital zircons. *Earth Planet. Sci. Lett.* **2020**, *536*, 116140. [CrossRef]
10. Deng, Z.; Liu, S.; Zhang, W.; Hu, F.; Li, Q. Petrogenesis of the Guangtoushan granitoid suite, central China: Implications for Early Mesozoic geodynamic evolution of the Qinling Orogenic Belt. *Gondwana Res.* **2016**, *30*, 112–131. [CrossRef]
11. Dong, Y.P.; Santosh, M. Tectonic architecture and multiple orogeny of the Qinling Orogenic Belt, Central China. *Gondwana Res.* **2016**, *29*, 1–40. [CrossRef]
12. Dong, Y.P.; Liu, X.M.; Santosh, M.; Zhang, X.N.; Chen, Q.; Yang, C.; Yang, Z. Neoproterozoic subduction tectonics of the northwestern Yangtze Block in South China: Constrains from zircon U–Pb geochronology and geochemistry of mafic intrusions in the Hannan Massif. *Precambrian Res.* **2011**, *189*, 66–90. [CrossRef]
13. Dong, Y.P.; Zhang, G.W.; Neubauer, F.; Liu, X.M.; Genser, J.; Hauzenberger, C. Tectonic evolution of the Qinling orogen, China: Review and synthesis. *J. Asian Earth Sci.* **2011**, *41*, 213–237. [CrossRef]
14. Dong, Y.P.; Yang, Z.; Liu, X.; Zhang, X.; He, D.; Li, W.; Zhang, F.; Sun, S.; Zhang, H.; Zhang, G. Neoproterozoic amalgamation of the Northern Qinling terrain to the North China Craton: Constraints from geochronology and geochemistry of the Kuanping ophiolite. *Precambrian Res.* **2014**, *255*, 77–95. [CrossRef]
15. Dong, Y.P.; Sun, S.; Yang, Z.; Liu, X.; Zhang, F.; Li, W.; Cheng, B.; He, D.; Zhang, G. Neoproterozoic subduction-accretionary tectonics of the South Qinling Belt, China. *Precambrian Res.* **2017**, *293*, 73–90. [CrossRef]

16. Zhang, G.W.; Zhang, Z.Q.; Dong, Y.P. Nature of main tectono-lithostratigraphic units of the Qinling orogen: Implications for the tectonic evolution. *Acta Petrol. Sin.* **1995**, *11*, 101–114. (In Chinese with English Abstract)
17. Zhang, G.W.; Guo, A.L.; Yao, A.P. Western Qinling -Songpan continental tectonic node in China's continental tectonics. *Earth Sci. Front.* **2004**, *11*, 23–32. (In Chinese with English Abstract)
18. Bao, Z.W.; Wang, Q.; Bai, G.D.; Zhao, Z.H.; Song, Y.W.; Liu, X.M. Geochronology and geochemistry of the Fangcheng Neoproterozoic alkali-syenites in East Qinling orogen and its geodynamic implications. *Sci. Bull.* **2008**, *53*, 2050–2061. [CrossRef]
19. Liu, B.X.; Nie, H.; Qi, Y.; Yang, L.; Zhu, X.Y.; Chen, F.K. Genesis and geological significances of Neoproterozoic granitoids in the North Qinling terrain, SW Henan, China. *Acta Petrol. Sin.* **2013**, *29*, 2437–2455. (In Chinese with English Abstract)
20. Wang, F.; Zhu, L.; Li, J.; Lee, B.; Gong, H.; Yang, T.; Wang, W.; Xu, A. Zircon U-Pb ages and Hf isotopic characteristics of the Dehe biotite monzonitic gneiss pluton in the North Qinling orogen and their geological significance. *Chin. J. Geochem.* **2011**, *30*, 204–216. [CrossRef]
21. Gao, S.; Zhang, B.R.; Wang, D.P.; Ouyang, J.P.; Xie, Q.L. Geochemical evidence for the Proterozoic tectonic evolution of the Qinling Orogenic Belt and its adjacent margins of the North China and Yangtze cratons. *Precambrian Res.* **1996**, *80*, 23–48. [CrossRef]
22. Xu, J.F.; Castillo, P.R.; Li, X.H.; Yu, X.Y.; Zhang, B.R.; Han, Y.W. MORB-type rocks from the Paleo-Tethyan Mian-Lueyang northern ophiolite in the Qinling Mountains, central China: Implications for the source of the low 206Pb/204Pb and high 143Nd/144Nd mantle component in the Indian Ocean. *Earth Planet. Sci. Lett.* **2002**, *198*, 323–337. [CrossRef]
23. Li, S.Z.; Jahn, B.M.; Zhao, S.J.; Dai, L.M.; Li, X.Y.; Suo, Y.H.; Guo, L.L.; Wang, Y.L.; Liu, X.C.; Lan, H.Y.; et al. Triassic southeastward subduction of North China Block to South China Block: Insights from new geological, geophysical and geochemical data. *Earth-Sci. Rev.* **2017**, *166*, 270–285. [CrossRef]
24. Qiu, K.F.; Yu, H.C.; Gou, Z.Y.; Liang, Z.L.; Zhang, J.L.; Zhu, R. Nature and origin of Triassic igneous activity in the Western Qinling Orogen: The Wenquan composite pluton example. *Int. Geol. Rev.* **2018**, *60*, 242–266. [CrossRef]
25. Jin, X.Y.; Li, J.W.; Hofstra, A.H.; Sui, J.X. Magmatic-hydrothermal origin of the early triassic laodou lode gold deposit in the xiahe-hezuo district, west qinling orogen, china: Implications for gold metallogeny. *Miner. Depos.* **2017**, *52*, 883–902. [CrossRef]
26. Li, W.Y. Geochronology and Geochemistry of the Ophiolites and Island-Arc-Type Igneous Rocks in the Western Qinling Orogen and the Eastern Kunlun Orogen: Implication for the Evolution of the Tethyan Ocean. Ph.D. Thesis, University of Science and Technology of China, Hefei, China, 2008; pp. 1–154. (In Chinese with English Abstract)
27. Liang, X.; Liu, X.M.; He, D.F.; Dong, Y.P.; Yang, Z. Fabrics and geochronology of the Wushan ductile shear zone: Tectonic implications for the Shangdan suture zone in the Qinling orogen, Central China. *J. Asian Earth Sci.* **2017**, *139*, 71–82. [CrossRef]
28. Pei, X.Z.; Ding, S.P.; Zhang, G.; Liu, H.B.; Li, Z.C.; Li, W.Y.; Liu, Z.Q.; Meng, Y. Zircons LA-ICP-MS U-Pb Dating of Neoproterozoic Granitoid Gneisses in the North Margin of West Qinling and Geological Implication. *Acta Geol. Sin.* **2007**, *81*, 772–786. (In Chinese with English Abstract)
29. Liu, H.B.; Pei, X.Z.; Ding, S.P.; Li, Z.C.; Sun, R.Q. LA- ICP- MS zircon U- Pb dating of the Neoproterozoic gr anitic gneisses in the Yuanlong area, Tianshui City, West Qinling, China, and their geological significance. *Geol. Bull. China* **2006**, *25*, 1315–1320. (In Chinese with English Abstract)
30. Li, S.G.; Chen, Y.Z.; Zhang, G.W.; Zhang, Z.Q. A 1GA B.P. Alpine peridotite body emplaced into the Qinling Group: Evidence for the existence of the late proterozoic plate tectonics in the North Qinling area. *Geol. Rev.* **1991**, *37*, 235–242. (In Chinese with English Abstract)
31. Chen, Z.H.; Lu, S.N.; Li, H.K.; Song, B.; Li, H.M.; Xiang, Z.Q. The age of Dehe biotite monzogranite gneiss in the North Qinling: TIMS and SHRIMP U-Pb zircon dating. *Geol. Bull. China* **2004**, *23*, 136–141. (In Chinese with English Abstract)
32. Zhang, C.L.; Liu, L.; Zhang, G.W.; Wang, T.; Chen, D.L.; Yuan, H.L.; Liu, X.M.; Yan, Y.X. Determination of Neoproterozoic post-collisional granites in the north Qinling Mountains and its tectonic significance. *Earth Sci. Front.* **2004**, *11*, 33–42. (In Chinese with English Abstract)
33. Zhang, H.F.; Zhang, B.R.; Luo, T.C. Geochemical study of genesis and tectonic setting for late proterozoic granitoids, North Qinling, China. *Earth Sci. J. China Univ. Geosci.* **1993**, *18*, 194–202. (In Chinese with English Abstract)
34. Liu, J.F.; Sun, Y.; Sun, W.D. LA-ICP-MS zircon dating from the Lajimiao mafic complex in the Qinling orogenic belt. *Acta Petrol. Sin.* **2009**, *25*, 320–330. (In Chinese with English Abstract)
35. Chen, J.L.; Wang, Z.Q.; Xu, X.Y.; Zeng, Z.X.; Wang, H.L.; He, S.P.; Li, P. Geochemical characteristics and petrogenetic investigation of the Lianghekou granite pluton, northern Qinling Mountains. *Acta Petrologica Sinica.* **2007**, *23*, 1043–1054. (In Chinese with English Abstract)
36. Wang, T.; Li, W.P.; Wang, X.X. Zircon U-Pb age of the niujiaoshan granitoid gneisses in the Qinling complex of the Qinling orogenic belt-with a discussion of its geological significance. *Reg. Geol. China* **1998**, *17*, 262–265. (In Chinese with English Abstract)
37. Lu, S.N.; Chen, Z.H.; Li, H.K.; Hao, G.J.; Xiang, Z.Q. Two Magmatic Belts of the Neoproterozoic in the Qinling Orogenic Belt. *Acta Petrol. Sin.* **2005**, *79*, 165–173. (In Chinese with English Abstract)
38. Wang, T.; Zhang, Z.Q.; Wang, X.X.; Wang, Y.B.; Zhang, C.L. Neoproterozoic Collisional Deformation in the Core of the Qinling Orogen and Its Age: Constrained by Zircon SHRIMP Dating of Strongly Deformed Syn-collisional Granites and Weakly Deformed Granitic Veins. *Acta Petrol. Sin.* **2005**, *79*, 220–231. (In Chinese with English Abstract)
39. Chen, D.L.; Liu, L.; Sun, Y.; Zhang, A.D.; Zhang, C.L.; Liu, X.M.; Luo, J.H. Determination of the Neoproterozoic Shicaogou Syn-collisional Granite in the Eastern Qinling Mountains and Its Geological Implications. *Acta Geol. Sin.* **2004**, *78*, 73–82.

40. Chen, Z.H.; Lu, S.N.; Li, H.K.; Li, H.M.; Xiang, Z.Q.; Zhou, H.Y.; Song, B. Constraining the role of the Qinling orogen in the assembly and break-up of Rodinia: Tectonic implications for Neoproterozoic granite occurrences. *J. Asian Earth Sci.* **2006**, *28*, 99–115. [CrossRef]
41. Wu, P.; Wu, Y.B.; Zhou, G.Y.; Zhang, W.X.; He, Y. Geochronology, geochemistry, and isotope compositions of "Grenvillian" S-type granites in the North Qinling unit, central China: Petrogenesis and tectonic significance. *Precambrian Res.* **2021**, *360*, 106247. [CrossRef]
42. Gong, X.K.; Chen, D.L.; Ren, Y.F.; Luo, F.H.; Tan, J.; Muredili, M.; Li, K. Geochronology and geochemistry of the Mashankou pluton in the eastern Qinling Group: Implications for the Early Neoproterozoic tectonic evolution of the North Qinling orogeny. *Acta Geol. Sin.* **2021**, *3*, 1–20. (In Chinese with English Abstract)
43. Meng, Q.R.; Zhang, G.W. Timing of the North and South China blocks: Controversy reconciliation. *Geol. Soc. Am. Bull.* **1999**, *27*, 123. [CrossRef]
44. Luo, B.; Zhang, H.; Lü, X. U–Pb zircon dating, geochemical and Sr–Nd–Hf isotopic compositions of Early Indosinian intrusive rocks in West Qinling, central China: Petrogenesis and tectonic implications. *Contrib. Mineral. Petrol.* **2012**, *164*, 551–569. [CrossRef]
45. Hu, J.Q.; Li, X.W.; Xu, J.F.; Mo, X.X.; Wang, F.Y.; Yu, H.X.; Shan, W.; Xing, H.Q.; Huang, X.F.; Dong, G.C. Generation of coeval metaluminous and muscovite-bearing peraluminous granitoids in the same composite pluton in West Qinling, NE Tibetan Plateau. *Lithos* **2019**, *344–345*, 374–392. [CrossRef]
46. Liu, H.N.; Li, X.W.; Mo, X.X.; Xu, J.F.; Liu, J.J.; Dong, G.C.; Shan, W.; Zhang, Y.; Wang, K.; Yu, H.X. Early Mesozoic crustal evolution in the NW segment of West Qinling, China: Evidence from diverse intermediate–felsic igneous rocks. *Lithos* **2021**, *396–397*, 106187. [CrossRef]
47. Xing, H.Q.; Li, X.W.; Xu, J.F.; Mo, X.X.; Shan, W.; Yu, H.X.; Hu, J.Q.; Huang, X.F.; Dong, G.-C. The genesis of felsic magmatism during the closure of the Northeastern Paleo-Tethys Ocean: Evidence from the Heri batholith in West Qinling, China. *Gondwana Res.* **2020**, *84*, 38–51. [CrossRef]
48. Wang, X.X.; Wang, T.; Zhang, C. Neoproterozoic, Paleozoic, and Mesozoic granitoid magmatism in the Qinling Orogen, China: Constraints on orogenic process. *J. Asian Earth Sci.* **2013**, *72*, 129–151. [CrossRef]
49. Wang, X.X.; Wang, T.; Zhang, C. Granitoid magmatism in the Qinling orogen, central China and its bearing on orogenic evolution. *Sci. China Earth Sci.* **2015**, *58*, 1497–1512. [CrossRef]
50. Zhang, J.; Zhang, H.F.; Li, L. Neoproterozoic tectonic transition in the South Qinling Belt: New constraints from geochemistry and zircon U–Pb–Hf isotopes of diorites from the Douling Complex. *Precambrian Res.* **2018**, *306*, 112–128. [CrossRef]
51. Zhu, Y.X.; Wang, L.X.; Ma, C.Q.; Wiedenbeck, M.; Wang, W. The Neoproterozoic alkaline rocks from Fangcheng area, East Qinling (China) and their implications for regional Nb mineralization and tectonic evolution. *Precambrian Res.* **2020**, *350*, 105852. [CrossRef]
52. Liu, C.J.; Pei, X.Z.; Li, Z.C.; Li, R.B.; Pei, L.; Gao, J.M.; Wei, F.H.; Wang, Y.C.; Wu, S.K.; Chen, Y.X. Geochemical features and tec tonic setting of the Neoproterozoic granitic gneiss in Tianshui area on the northern margin of West Qinling. *Geol. Bull. China* **2012**, *31*, 1588–1601. (In Chinese with English Abstract)
53. Chen, H.J.; Wu, C.L.; Lei, M.; Guo, W.F.; Zhang, X.; Zheng, K.; Gao, D.; Wu, D. Petrogenesis and implications for Neoproterozoic granites in Kekesayi Area, South Altyn continent. *Earth Sci.* **2018**, *43*, 1278–1292. (In Chinese with English Abstract)
54. Gao, Y.L.; Zhao, J.; Long, X.P. Geochemistry of Neoproterozoic S-type granites from the Maxianshan group in the Qilian Orogenic Belt and its geological implications. *J. Northwest Univ.* **2021**, *51*, 969–984. (In Chinese with English Abstract)
55. He, D.F.; Dong, Y.P.; Liu, X.M.; Zhou, X.H.; Zhang, F.F.; Sun, S.S. Zircon U–Pb geochronology and Hf isotope of granitoids in East Kunlun: Implications for the Neoproterozoic magmatism of Qaidam Block, Northern Tibetan Plateau. *Precambrian Res.* **2018**, *314*, 377–393. [CrossRef]
56. Liu, D.L.; Jiang, S.Y.; Li, W.T.; Shi, M. Neoproterozoic and Paleozoic tectonic evolution in north Qaidam, northeastern Tibetan Plateau recorded by magmatism and metamorphism. *Gondwana Res.* **2022**, *103*, 84–104. [CrossRef]
57. Peng, Y.B.; Yu, S.Y.; Li, S.Z.; Zhang, J.X.; Liu, Y.J.; Li, Y.S.; Santosh, M. Early Neoproterozoic magmatic imprints in the Altun-Qilian-Kunlun region of the Qinghai-Tibet Plateau: Response to the assembly and breakup of Rodinia supercontinent. *Earth-Sci. Rev.* **2019**, *199*, 102954. [CrossRef]
58. Song, S.G.; Su, L.; Li, X.H.; Niu, Y.L.; Zhang, L.F. Grenville-age orogenesis in the Qaidam-Qilian block: The link between South China and Tarim. *Precambrian Res.* **2012**, *220–221*, 9–22. [CrossRef]
59. Tung, K.A.; Yang, H.Y.; Liu, D.Y.; Zhang, J.X.; Yang, H.J.; Shau, Y.H.; Tseng, C.Y. The Neoproterozoic granitoids from the Qilian block, NW China: Evidence for a link between the Qilian and South China blocks. *Precambrian Res.* **2013**, *235*, 163–189. [CrossRef]
60. Wu, D.Q.; Sun, F.Y.; Pan, Z.C.; Yu, L.; Li, L.; Gao, H.C.; Tian, N.; Xu, C.H. Neoproterozoic magmatic and metamorphic imprints in the East Kunlun Orogenic Belt, North Tibetan Plateau, NW China: Implications for the assembly and initial breakup of the Rodinia supercontinent. *Precambrian Res.* **2021**, *354*, 106076. [CrossRef]
61. Yu, S.Y.; Zhang, J.X.; del Real, P.G.; Zhao, X.L.; Hou, K.J.; Gong, J.H.; Li, Y.S. The Grenvillian orogeny in the Altun–Qilian–North Qaidam mountain belts of northern Tibet Plateau: Constraints from geochemical and zircon U–Pb age and Hf isotopic study of magmatic rocks. *J. Asian Earth Sci.* **2013**, *73*, 372–395. [CrossRef]

62. Dong, Y.P.; Zhou, M.F.; Zhang, G.W.; Zhou, D.W.; Liu, L.; Zhang, Q. The Grenvillian Songshugou ophiolite in the Qinling Mountains, Central China: Implications for the tectonic evolution of the Qinling orogenic belt. *J. Asian Earth Sci.* **2008**, *32*, 325–335. [CrossRef]
63. Nie, H.; Yang, J.Z.; Zhou, G.Y.; Liu, C.Z.; Zheng, J.P.; Zhang, W.X.; Zhao, Y.J.; Wang, H.; Wu, Y.B. Geochemical and Re–Os isotope constraints on the origin and age of the Songshugou peridotite massif in the Qinling orogen, central China. *Lithos* **2017**, *292–293*, 307–319. [CrossRef]
64. Sun, S.S.; Dong, Y.P.; Sun, Y.L.; Cheng, C.; Huang, X.X.; Liu, X.M. Re-Os geochronology, O isotopes and mineral geochemistry of the Neoproterozoic Songshugou ultramafic massif in the Qinling Orogenic Belt, China. *Gondwana Res.* **2019**, *70*, 71–87. [CrossRef]
65. Yu, H.; Zhang, H.F.; Santosh, M. Mylonitized peridotites of Songshugou in the Qinling orogen, central China: A fragment of fossil oceanic lithosphere mantle. *Gondwana Res.* **2017**, *52*, 1–17. [CrossRef]
66. Zhang, H.F.; Yu, H. Petrological and Tectonic Evolution of Orogenic Peridotite Massif: A Case of Songshugou Peridotites. *Earth Sci.* **2019**, *44*, 1057–1066. (In Chinese with English Abstract)
67. Cao, Y.; Song, S.G.; Su, L.; Jung, H.; Niu, Y.L. Highly refractory peridotites in Songshugou, Qinling orogen: Insights into partial melting and melt/fluid–rock reactions in forearc mantle. *Lithos* **2016**, *252–253*, 234–254. [CrossRef]
68. Chen, D.L.; Liu, L. New data on the chronology of eclogite and associated rock from Guanpo Area, North Qinling orogeny and its constraint on nature of North Qinling HP-UHP eclogite terrane. *Earth Sci. Front.* **2011**, *18*, 158–169.
69. Chen, D.L.; Ren, Y.F.; Gong, X.K.; Liu, L.; Gao, S. Identification and its geological significance of eclogite in Songshugou, the North Qinling. *Acta Petrol. Sin.* **2015**, *31*, 1841–1854. (In Chinese with English Abstract)
70. Liao, X.Y.; Liu, L.; Wang, Y.W.; Cao, Y.T.; Chen, D.L.; Dong, Y.P. Multi-stage metamorphic evolution of retrograde eclogite with a granulite-facies overprint in the Zhaigen area of the North Qinling Belt, China. *Gondwana Res.* **2016**, *30*, 79–96. [CrossRef]
71. Yu, H.; Zhang, H.-F.; Li, X.-H.; Zhang, J.; Santosh, M.; Yang, Y.-H.; Zhou, D.-W. Tectonic evolution of the North Qinling Orogen from subduction to collision and exhumation: Evidence from zircons in metamorphic rocks of the Qinling Group. *Gondwana Res.* **2016**, *30*, 65–78. [CrossRef]
72. Wang, H.; Wu, Y.B.; Gao, S.; Liu, X.C.; Gong, H.J.; Li, Q.L.; Li, X.H.; Yuan, H.L. Eclogite origin and timings in the North Qinling terrane, and their bearing on the amalgamation of the South and North China Blocks. *J. Metamorph. Geol.* **2011**, *29*, 1019–1031. [CrossRef]
73. Wang, H.; Wu, Y.-B.; Gao, S.; Liu, X.-C.; Liu, Q.; Qin, Z.-W.; Xie, S.-W.; Zhou, L.; Yang, S.-H. Continental origin of eclogites in the North Qinling terrane and its tectonic implications. *Precambrian Res.* **2013**, *230*, 13–30. [CrossRef]
74. Li, X.H.; Long, W.G.; Li, Q.L.; Liu, Y.; Zheng, Y.F.; Yang, Y.H.; Chamberlain, K.R.; Wan, D.F.; Guo, C.H.; Wang, X.C.; et al. Penglai Zircon Megacrysts: A Potential New Working Reference Material for Microbeam Determination of Hf-O Isotopes and U-Pb Age. *Geostand. Geoanalytical Res.* **2010**, *34*, 117–134. [CrossRef]
75. Li, X.H.; Tang, G.Q.; Gong, B.; Yang, Y.H.; Hou, K.J.; Hu, Z.; Li, Q.; Liu, Y.; Li, W. Qinghu zircon: A working reference for microbeam analysis of U-Pb age and Hf and O isotopes. *Chin. Sci. Bull.* **2013**, *58*, 4647–4654. [CrossRef]
76. Yang, Q.; Xia, X.; Zhang, W.; Zhang, Y.; Xiong, B.; Xu, Y.; Wang, Q.; Wei, G. An evaluation of precision and accuracy of SIMS oxygen isotope analysis. *Solid Earth Sci.* **2018**, *3*, 81–86. [CrossRef]
77. Yang, Q.; Xia, X.P.; Zhang, L.; Zhang, W.; Zhang, Y.; Chen, L.; Yang, Y.; He, M. Oxygen isotope homogeneity assessment for apatite U-Th-Pb geochronology reference materials. *Surf. Interface Anal.* **2019**, *52*, 197–213. [CrossRef]
78. Yuan, H.L.; Gao, S.; Liu, X.M.; Li, H.M.; Günther, D.; Wu, F.Y. Accurate U-Pb Age and Trace Element Determinations of Zircon by Laser Ablation-Inductively Coupled Plasma-Mass Spectrometry. *Geostand. Geoanalytical Res.* **2004**, *28*, 353–370. [CrossRef]
79. Andersen, T. Correction of common lead in U–Pb analyses that do not report ^{204}Pb. *Chem. Geol.* **2002**, *192*, 59–79. [CrossRef]
80. Ludwig, K.R. *Isoplot 3.00: A Geochronological Toolkit for Microsoft Excel*; Berkeley Geochronology Center: Berkeley, CA, USA, 2003.
81. Chu, N.-C.; Taylor, R.N.; Chavagnac, V.r.; Nesbitt, R.W.; Boella, R.M.; Milton, J.A.; German, C.R.; Bayon, G.; Burton, K. Hf isotope ratio analysis using multi-collector inductively coupled plasma mass spectrometry: An evaluation of isobaric interference corrections. *J. Anal. At. Spectrom.* **2002**, *17*, 1567–1574. [CrossRef]
82. Blichert-Toft, J.; Albarède, F. The Lu-Hf isotope geochemistry of chondrites and the evolution of the mantle-crust system. *Earth Planet. Sci. Lett.* **1997**, *148*, 243–258. [CrossRef]
83. Griffin, W.L.; Pearson, J.N.; Belousova, E.; Jackson, E.S. The Hf isotope composition of cratonic mantle: LAM-MC-ICPMS analysis of zircon megacrysts in kimberlites. *Geochim. Cosmochim. Acta* **2000**, *64*, 133–147. [CrossRef]
84. Wu, F.Y.; Li, X.H.; Zheng, Y.F.; Gao, S.J.A.P.S. Lu-Hf isotopic systematics and thier applications in petrology. *Acta Petrol. Sin.* **2007**, *23*, 185–220. (In Chinese with English Abstract)
85. Middlemost, E. Naming materials in the magma/igneous rock system. *Earth-Sci. Rev.* **1994**, *37*, 215–224. [CrossRef]
86. Peccerillo, A.; Taylor, S.R. Geochemistry of Eocene calc-alkaline volcanic rocksfrom the Kastamonu area, Northern Turkey. *Contrib. Mineral. Petrol.* **1976**, *58*, 63–81. [CrossRef]
87. Maniar, P.D.; Piccoli, P.M. Tectonic discrimination of granitoids. *Geol. Soc. Am. Bull.* **1989**, *101*, 635–643. [CrossRef]
88. Corfu, F.; Hanchar, J.M.; Hoskin, P.W.O.; Kinny, P. Atlas of Zircon Textures. *Rev. Mineral. Geochem.* **2003**, *53*, 469–500. [CrossRef]
89. Hoskin, P.W. Trace-element composition of hydrothermal zircon and the alteration of Hadean zircon from the Jack Hills, Australia. *Geochim. Cosmochim. Acta* **2005**, *69*, 637–648. [CrossRef]
90. Schulz, B.; Klemd, R.; Brätz, H. Host rock compositional controls on zircon trace element signatures in metabasites from the Austroalpine basement. *Geochim. Cosmochim. Acta* **2006**, *70*, 697–710. [CrossRef]

91. Jung, S.; Hoernes, S.; Mezger, K. Geochronology and petrology of migmatites from the Proterozoic Damara Belt—importance of episodic fluid-present disequilibrium melting and consequences for granite petrology. *Lithos* **2000**, *111*, 220–235. [CrossRef]
92. Patiño Douce, A.E.; Johnston, A.D. Phase equilibria and melt productivity in the pelitic system: Implications for the origin of peraluminous granitoids and aluminous granulites. *Contrib. Mineral. Petrol.* **1991**, *107*, 202–218. [CrossRef]
93. Montel, J.M.; Vielzeuf, D. Partial melting of metagreywackes, Part II. Compositions of minerals and melts. *Contrib. Mineral. Petrol.* **1997**, *128*, 176–196. [CrossRef]
94. Vielzeuf, D.; Montel, J.M. Partial melting of metagreywackes. Part I. Fluid-absent experiments and phase relationships. *Contrib. Mineral. Petrol.* **1994**, *117*, 375–393. [CrossRef]
95. Clemens, J.D. Granitic magmas with I-type affinities, from mainly metasedimentary sources: The Harcourt batholith of southeastern Australia. *Contrib. Mineral. Petrol.* **2018**, *173*, 11. [CrossRef]
96. Chappell, B.W.; Bryant, C.J.; Wyborn, D. Peraluminous I-type granites. *Lithos* **2012**, *153*, 142–153. [CrossRef]
97. Valley, J.W.; Lackey, J.S.; Cavosie, A.J.; Clechenko, C.C.; Spicuzza, M.J.; Basei, M.A.S.; Bindeman, I.N.; Ferreira, V.P.; Sial, A.N.; King, E.M.; et al. 4.4 billion years of crustal maturation: Oxygen isotope ratios of magmatic zircon. *Contrib. Mineral. Petrol.* **2005**, *150*, 561–580. [CrossRef]
98. Kemp, A.I.; Hawkesworth, C.J.; Foster, G.L.; Paterson, B.A.; Woodhead, J.D.; Hergt, J.M.; Gray, C.M.; Whitehouse, M.J. Magmatic and crustal differentiation history of granitic rocks from hf-o isotopes in zircon. *Science* **2007**, *315*, 980–983. [CrossRef] [PubMed]
99. Kang, W.B.; Li, W.; Dong, Y.P.; Zhang, L.; Zhao, J.X.; Sheir, F. Multi-stage metamorphism and deformation of the North Qinling Orogenic Belt: Constraints from petrology, geochronology, and structural analysis of the Qinling Complex. *Gondwana Res.* **2022**, *105*, 201–216. [CrossRef]
100. Li, C.; Ren, L.; Zong, S.; Wang, Y.; Li, M. Confirmation of the Major Grenville Event in the Qinling Complex of the Qinling Orogenic Belt, Central China. *J. Earth Sci.* **2019**, *30*, 494–509. [CrossRef]
101. Grimes, C.B.; Ushikubo, T.; Kozdon, R.; Valley, J.W. Perspectives on the origin of plagiogranite in ophiolites from oxygen isotopes in zircon. *Lithos* **2013**, *179*, 48–66. [CrossRef]
102. Wei, C.S.; Zhao, Z.F.; Spicuzza, M.J. Zircon oxygen isotopic constraint on the sources of late Mesozoic A-type granites in eastern China. *Chem. Geol.* **2008**, *250*, 1–15. [CrossRef]
103. Appleby, S.K.; Gillespie, M.R.; Graham, C.M.; Hinton, R.W.; Oliver, G.; Kelly, N.M.; Mineralogy, E.J.C.t. Do S-type granites commonly sample infracrustal sources? New results from an integrated O, U-Pb and Hf isotope study of zircon. *Contrib. Mineral. Petrol.* **2010**, *160*, 115–132. [CrossRef]
104. Bindeman, I.N.; Fu, B.; Kita, N.T.; Valley, J.W. Origin and Evolution of Silicic Magmatism at Yellowstone Based on Ion Microprobe Analysis of Isotopically Zoned Zircons. *J. Petrol.* **2008**, *49*, 163–193. [CrossRef]
105. Sylvester, P.J. Post-collisional strongly peraluminous granites. *Lithos* **1998**, *45*, 29–44. [CrossRef]
106. Bader, T.; Ratschbacher, L.; Franz, L.; Yang, Z.; Hofmann, M.; Linnemann, U.; Yuan, H.J.T. The heart of China revisited, I. Proterozoic tectonics of the Qin mountains in the core of supercontinent Rodinia. *Tectonics* **2013**, *32*, 661–687. [CrossRef]
107. Cao, H.H.; Li, S.; Zhao, S.Z.; Wang, P.C.; Somerville, I.; Wang, Q.; Yu, S. Precambrian tectonic affinity of the North Qinling Microcontinent: Constraints from the discovery of Mesoproterozoic magmatic zircons in the Qinling Group. *Geol. J.* **2017**, *52*, 142–154. [CrossRef]
108. Shi, Y.; Qiu, J.S.; Yu, J.H.; Xu, X.S.; Chen, L.H.J.A.P.S. Geochronology and geochemistry of the Qinling Group in the eastern Qinling Orogen. *Acta Petrol. Sin.* **2009**, *25*, 2651–2670, in Chinese with English abstract.
109. Shi, Y.; Huang, Q.; Liu, X.; Krapež, B.; Yu, J.; Bai, Z. Provenance and tectonic setting of the supra-crustal succession of the Qinling Complex: Implications for the tectonic affinity of the North Qinling Belt, Central China. *J. Asian Earth Sci.* **2018**, *158*, 112–139. [CrossRef]
110. Becker, H.; Jochum, K.P.; Carlson, R.W. Trace element fractionation during dehydration of eclogites from high-pressure terranes and the implications for element fluxes in subduction zones. *Chem. Geol.* **2000**, *163*, 65–99. [CrossRef]
111. Dostal, J.; Strong, D.F.; Jamieson, R.A. Trace element mobility in the mylonite zone within the ophiolite aureole, St. Anthony Complex, Newfoundland. *Earth Planet. Sci. Lett.* **1980**, *49*, 188–192. [CrossRef]
112. Pearce, J.A. Geochemical Fingerprinting of the Earth's Oldest Rocks. *Geology* **2014**, *42*, 175–176. [CrossRef]
113. Polat, A.; Hofmann, A.W. Alteration and geochemical patterns in the 3.7–3.8 Ga Isua greenstone belt, West Greenland. *Precambrian Res.* **2003**, *126*, 197–218. [CrossRef]
114. Clemens, J.D.; Stevens, G.J.L. What controls chemical variation in granitic magmas? *Lithos* **2012**, *134–135*, 317–329. [CrossRef]
115. Zheng, Y.F.; Gao, P. The production of granitic magmas through crustal anatexis at convergent plate boundaries. *Lithos* **2021**, *402–403*, 106232. [CrossRef]
116. Castro, A.; Douce, A.; Corretgé, L.; Rosa, J.; El-Biad, M.; El-Hmidi, H.J.C.t.M. Origin of peraluminous granites and granodiorites, Iberian massif, Spain: An experimental test of granite petrogenesis. *Contrib. Mineral. Petrol.* **1999**, *135*, 255–276. [CrossRef]
117. Gray, C.M.; Letters, P.S. An isotopic mixing model for the origin of granitic rocks in southeastern Australia. *Earth Planet. Sci. Lett.* **1984**, *70*, 47–60. [CrossRef]
118. Patiño Douce, A.E. Experimental generation of hybrid silicic melts by reaction of high-Al basalt with metamorphic rocks. *J. Geophys. Res. Solid Earth* **1995**, *100*, 15623–15639. [CrossRef]
119. Patiño Douce, A.E.; Harris, N. Experimental Constraints on Himalayan Anatexis. *J. Petrol.* **1998**, *39*, 689–710. [CrossRef]

120. Thompson, A.B. Dehydration melting of pelitic rocks and the generation of H_2O-undersaturated granitic liquids. *Am. J. Sci.* **1982**, *282*, 1567–1595. [CrossRef]
121. Brown, M. Crustal melting and melt extraction, ascent and emplacement in orogens: Mechanisms and consequences. *J. Geol. Soc.* **2007**, *164*, 709–730. [CrossRef]
122. Stevens, G.; Clemens, J.D. Comment on 'Water-fluxed melting of the continental crust: A review' by RF Weinberg and P. Hasalova. *Lithos* **2015**, *212–215*, 158–188.
123. Weinberg, R.F.; Hasalová, P. Water-fluxed melting of the continental crust: A review. *Lithos* **2015**, *212–215*, 158–188. [CrossRef]
124. Watson, E.B.; Harrison, T.M. Zircon saturation revisited: Temperature and composition effects in a variety of crustal magma types. *Earth Planet. Sci. Lett.* **1983**, *64*, 295–304. [CrossRef]
125. Ferry, J.M.; Watson, E.B. New thermodynamic models and revised calibrations for the Ti-in-zircon and Zr-in-rutile thermometers. *Contrib. Mineral. Petrol.* **2007**, *154*, 429–437. [CrossRef]
126. Watson, E.B.; Harrison, T.M. Zircon Thermometer Reveals Minimum Melting Conditions on Earliest Earth. *Science* **2005**, *308*, 841–844. [CrossRef] [PubMed]
127. Watson, E.B.; Wark, D.A.; Thomas, J.B. Crystallization thermometers for zircon and rutile. *Contrib. Mineral. Petrol.* **2006**, *151*, 413–433. [CrossRef]
128. Schiller, D.; Finger, F. Application of Ti-in-zircon thermometry to granite studies: Problems and possible solutions. *Contrib. Mineral. Petrol.* **2019**, *174*, 51. [CrossRef]
129. Miller, C.F.; McDowell, S.M.; Mapes, R.W. Hot and cold granites? Implications of zircon saturation temperatures and preservation of inheritance. *Geology* **2003**, *31*, 529. [CrossRef]
130. Green, T.H. Anatexis of mafic crust and high-pressure crystallization of andesite. *Am. Soc. Mech. Eng.* **1982**, 465–487.
131. Moyen, J.F.; Stevens, G. Experimental Constraints on TTG Petrogenesis: Implications for Archean Geodynamics. *Geophys. Monogr. Ser.* **2006**, *164*, 149–175.
132. Wu, F.Y.; Li, X.H.; Yang, J.H.; Zheng, Y.F. Discussions on the petrogenesis of granites. *Acta Petrol. Sin.* **2007**, *23*, 1217–1238. (In Chinese with English Abstract)
133. Stevens, G.; Clemens, J.D.; Droop, G.T.R. Melt production during granulite-facies anatexis: Experimental data from "primitive" metasedimentary protoliths. *Contrib. Mineral. Petrol.* **1997**, *128*, 352–370. [CrossRef]
134. Veronique, G.; Bruce, T.A.; Peter, U. Melting of Biotite + Plagioclase + Quartz Gneisses: The Role of H_2O in the Stability of Amphibole. *J. Petrol.* **2000**, *5*, 651–666.
135. Pearce, J.A.; Harris, N.B.W.; Tindle, A.G. Trace Element Discrimination Diagrams for the Tectonic Interpretation of Granitic Rocks. *J. Petrol.* **1984**, *25*, 956–983. [CrossRef]
136. Liu, L.; Liao, X.; Zhang, C.; Chen, D.; Gong, X.; Kang, L. Multi-metamorphic timings of HP-UHP rocks in the North Qinling and their geological implications. *Acta Petrol. Sin.* **2013**, *29*, 1634–1656. (In Chinese with English Abstract)
137. Harris, N.B.; Pearce, J.A.; Tindle, A.G. Geochemical characteristics of collision-zone magmatism. *Geol. Soc. Lond. Spec. Publ.* **1986**, *19*, 67–81. [CrossRef]
138. Pitcher, W.S. Granite type and tectonic environment. In *Symposium on Mountain Building*; Academic Press: London, UK, 1983; pp. 19–40.
139. Diwu, C.R.; Long, X.P. Tectonic evolution of the North Qinling Orogenic Belt, Central China: Insights from metamafic rocks of the Songshugou Complex. *Geol. J.* **2018**, *54*, 2382–2399. [CrossRef]